Astronomy & Astrophysics manuscript no. output
July 12, 2026

From filaments to the hub: Gas kinematics and massive star formation in G329.34+0.14

Wenjun Zhang[1,2], Jianjun Zhou[1,2,3⋆], Tie Liu[4⋆⋆], Xunchuan Liu[4], Dongting Yang[5], Enrique Vázquez-Semadeni[6], Gilberto C. Gómez[6], Hongli Liu[5], Jarken Esimbek[1,2,3], Xindi Tang[1,2,3], Gang Wu[1,2,7], Siju Zhang[8], Di Li[9,10], Swagat Ranjan Das[8], Guido Garay[8,11], Fengwei Xu[12,13], N. K. Bhadari[12], Lokesh Dewangan[14], Prasanta Gorai[15,16], Jihye Hwang[17], Aiyuan Yang[9], James O. Chibueze[18,19], Pablo García[11,20], Chang Won Lee[17,21], Ariful Hoque[22], L. Viktor Tóth[23], Kee-Tae Kim[17], Willem Baan[1], Dalei Li[1,2,3], Yuxin He[1,2,3], Yingxiu Ma[1,3], Dongdong Zhou[1,3], Kadirya Tursun[1,3], Toktarkhan Komesh[1,24,25], and Weiguang Ji[1]

(Affiliations can be found after the references)

Received day month year; Accepted ...

ABSTRACT

We present ^{13}CO (J=2-1) emission from the SEDIGISM survey, together with ALMA Band 3 and Band 6 observations from the ATOMS and QUARKS surveys, to investigate the gas kinematics and feedback processes in the massive hub-filament system G329.34+0.14 (hereafter G329). Based on *Herschel* continuum morphology together with the ^{13}CO (J=2-1) integrated intensity and velocity distributions, a parsec-scale network of filaments was identified, converging toward the hub that hosts two massive clumps, MC 1 and MC 2, with respective masses of ∼4210 (±1259) $M_\odot$ and ∼1483 (±443) $M_\odot$. Position–velocity analysis reveals systematic projected velocity gradients along the filaments, consistent with organized gas motions on parsec scales and possible inflows toward the hub. Within MC 1, ALMA resolves a sub-parsec network of intra-hub filaments (IHFs) traced by H^{13}CO$^+$ (J=1-0), with a velocity organization similar to that seen on parsec scales. These IHFs are distributed around a central H II region, surrounded by a shell-like structure traced by CS (J=2-1) and H^{13}CO$^+$ (J=1-0) emission, with dense gas concentrated in its northeastern and southwestern sectors. The shell further shows SiO (J=2-1) and SO (J=3(2)-2(1)) emission, excited mainly by low-velocity shocks from the expansion of the H II region, with a minor contribution from protostellar outflows. Compared with the surrounding parsec-scale filaments, the IHFs are more compact but exhibit larger velocity gradients and line masses, suggesting that the inner hub gas is denser and dynamically more complex. MC 1 and MC 2 are interpreted as two massive clumps embedded in the same hub, with MC 1 appearing more evolved and more strongly affected by feedback than MC 2. G329 therefore provides an observational case in which the parsec-scale hub-filament structure and the dense IHF network show a broadly similar velocity organization. This suggests a possible kinematic connection between the surrounding filaments and dense gas in the hub interior.

Key words. star: formation – ISM: kinematics and dynamics – ISM: clouds – ISM: H II regions – ISM: individual objects: hub-filament system

1. Introduction

High-mass stars (> 8 $M_\odot$) are usually found within molecular clouds, and their strong feedback effects can significantly impact the surrounding gas structure. There is a long-standing debate about the formation process of high-mass stars, specifically how they acquire sufficient mass to form stars under intense feedback effects. The dense gas within molecular clouds, such as filaments, clumps, and cores, serves as a site for the formation of high-mass stars. Filaments are ubiquitous in the interstellar medium (ISM; André et al. 2010; Molinari et al. 2010a; Li et al. 2014, 2016; Mattern et al. 2018a; Wu et al. 2018), with three or more filaments intersecting to form a distinctive hub-filament system (HFS; Myers 2009). The hub exhibits a higher hydrogen column density than the filaments, while the filaments have a larger length-to-width ratio than the hub (Myers 2009; Schneider et al. 2012). Hub-filament systems are commonly described as networks of filaments converging toward dense central hubs, making them favorable sites for forming high-mass stars or star clusters (Liu et al. 2012; Peretto et al. 2013; Kumar et al. 2020; Xu et al. 2023).

Recent case studies and statistical surveys have established HFSs as important environments for high-mass star and young cluster formation (e.g., Peretto et al. 2013; Treviño-Morales et al. 2019; Kumar et al. 2020, 2022; Liu et al. 2023; Hacar et al. 2025). Longitudinal gas flows along filaments toward hubs have been reported in several HFSs, with typical inferred mass inflow rates of ∼10^{-4} to 10^{-3} $M_\odot$ year^{-1} (Yuan et al. 2018; Chen et al. 2019; Treviño-Morales et al. 2019; Liu et al. 2022a; Yang et al. 2023; Pan et al. 2024). Previous research has indicated that filaments within HFSs may play a crucial role in transporting material to the hubs, providing ample material for forming high-mass stars or star clusters within hubs (Peretto et al. 2013; Kumar et al. 2020). Most observational studies, however, still focus on parsec-scale filamentary gas dynamics. Probing sub-parsec structures and kinematics inside massive clumps is therefore essential, because filamentary gas may be reorganized into a denser network within hub clumps, closely associated with massive star and cluster formation (Kumar et al. 2022, 2025). Although a few recent studies have begun to probe HFSs down to clump and sub-parsec scales (Zhou et al. 2022; Yang et al. 2023; Xu et al. 2023; Liu et al. 2023; Pan et al. 2024), observational constraints on the internal gas kinematics of dense hubs remain limited. Such observations help relate the surrounding filamentary cloud to the denser, more evolved star-forming gas within the hub.

⋆ Corresponding author: e-mail: zhoujj@xao.ac.cn
⋆⋆ Corresponding author: e-mail: liutie@shao.ac.cn

Article published by EDP Sciences, to be cited as https://doi.org/10.1051/0004-6361/202554094

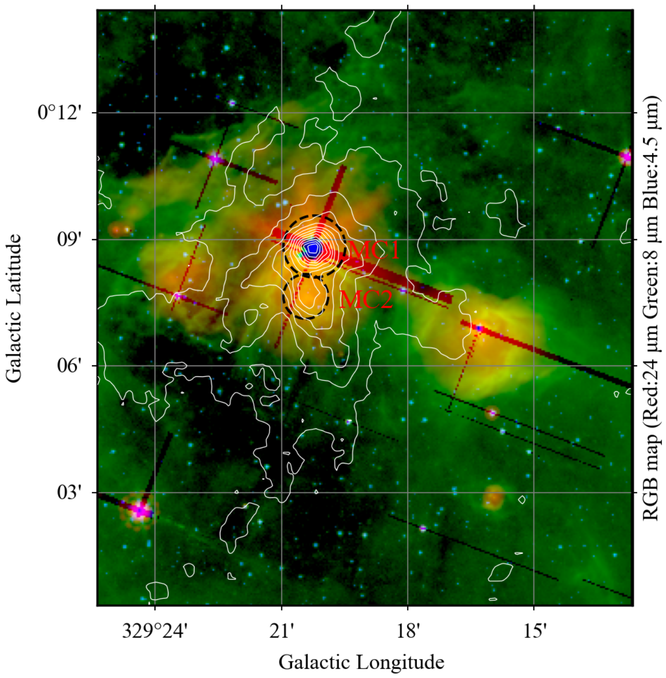

Fig. 1. RGB image of the G329 molecular cloud. Red represents 24 µm, green represents 8 µm, and blue represents 4.5 µm. The black circles indicate the 870 µm clumps (MC 1 and MC 2) observed by ATLASGAL (Urquhart et al. 2018), while the white contours show the integrated intensity of ^{13}CO (J=2-1), ranging from 5% to 93% of the peak value in 8% intervals.

The molecular cloud G329.34+0.14 (hereafter referred to as G329) exhibits a HFS morphology. Urquhart et al. (2018) identified two dense clumps located at the hub, AGAL329.337+00.147 (MC 1) and AGAL329.341+00.127 (MC 2) in the *Atacama Pathfinder Experiment* (APEX) Telescope Large Area Survey of the Galaxy (ATLASGAL) of 870 µm continuum emission (see Fig. 1). The luminosity-to-mass ratios of MC 1 and MC 2 are 147 and 6 $L_\odot$ $M_\odot{}^{-1}$, respectively; following the classification of Urquhart et al. (2018), these values place MC 1 at the massive-star-forming clump stage and MC 2 at the young-stellar-object-forming clump stage. Compared to MC 2, MC 1 exhibits stronger 4.5 µm and 8 µm emissions as well as a higher luminosity-to-mass ratio (see Fig. 1), indicating more intense stellar activity and a more advanced evolutionary stage in MC 1. Furthermore, ^{13}CO (J=2-1) high-velocity wings observed toward MC 1 suggest complex gas motions in the hub and motivate examining how the parsec-scale velocity field relates to the dense gas within MC 1 (Yang et al. 2022). The *Atacama Large Millimeter/submillimeter Array* (ALMA) Three-millimeter Observations of Massive Star-forming Regions (ATOMS) survey observed the massive star-forming region MC 1 (source ID: I15567-5236; Liu et al. 2020c,b). Liu et al. (2022b) report that the SiO (J=2-1) luminosity observed in MC 1 with the ATOMS Band-3 data is approximately 6.8×10^{-11} $L_\odot$, with a bolometric luminosity-to-mass ratio of about 158. The integrated intensity ratio of SiO (J=2-1) emission to H^{13}CO$^+$ (J=1-0) emission is approximately 0.38. Additionally, MC 1 is associated with $H_{40\alpha}$ radiation and outflows (Liu et al. 2022b). The SiO (J=2-1) emission features are spatially separated from $H_{40\alpha}$ emission and 3 mm continuum emission (Liu et al. 2022b, 2025). $H_{40\alpha}$ radiation indicates an ultracompact H II region within MC 1, with electron number densities of 1.49 and 1.63×10^4 cm^{-3} derived from $H_{40\alpha}$ recombination lines and 3 mm continuum emission, respectively. The temperature of the ultracompact H II region is approximately 6650 K (Zhang et al. 2023). SiO (J=2-1) emission is unrelated to the 3 mm continuum emission and appears around the ionized gas, suggesting that the detected SiO (J=2-1) radiation in MC 1 may originate from the expansion of the ultracompact H II region (Liu et al. 2025). Previous studies have shown that MC 1, located in the hub, has undergone intense star formation activity. The existing multiwavelength, high-resolution (∼0.3-37″) observations enable us to investigate the gas kinematics traced at different angular resolutions in G329. Therefore, studying the morphological structure and kinematic properties of the G329 molecular cloud and the central clump MC 1 provides key insights into the role of HFSs in star formation.

This work uses multiwavelength, high-resolution observations of the HFS G329 to investigate the gas kinematics of the parsec-scale filaments and the dense gas within MC 1, the more evolved massive clump in the hub. Our aim is to clarify how organized gas motions, massive star formation, and feedback are related in this system. In Sect. 2, we primarily present the observational data utilized in this study. Section 3 shows the main research findings. Section 4 discusses our research results, and Sect. 5 presents our main conclusions.

2. Observations

2.1. The CO spectral line data

The ^{13}CO (J=2-1) and C^{18}O (J=2-1) data used in this study were obtained from the Structure, Excitation, and Dynamics of the Inner Galactic Interstellar Medium (SEDIGISM) survey, which was conducted using the APEX telescope (Güsten et al. 2006). The SEDIGISM survey covers the Galactic plane within the range of $-60° \leq l \leq 18°$ and $|b| < 0.5°$ (Schuller et al. 2017). This survey includes the emission of both the ^{13}CO (J=2-1) and C^{18}O (J=2-1) molecular spectral lines. The data have an angular resolution of 30″ and a velocity resolution of 0.25 km s^{-1}. The sensitivity of the data is typically around 0.8-1.0 K at 1σ level (Mattern et al. 2018b).

2.2. ALMA data

We utilized data from the ATOMS survey, observed with the ALMA telescope (Project ID: 2019.1.00685.S; PI: Tie Liu). Detailed information can be found in Liu et al. (2020c) and Liu et al. (2020b). This project involved observations of 146 clumps in Band 3 using the Atacama Compact 7 m Array (ACA; Morita Array) and the 12 m array (C43-2 or C43-3 configurations) in single-pointing mode. The angular resolution and maximum recoverable scale of the ACA and the 12 m array are 13.3″ and 76.2″, and 1.7″ and 19.9″, respectively (Liu et al. 2020c). Eight spectral windows (SPWs) were used, covering 11 molecular transition lines, including H^{13}CN (J=1-0), H^{13}CO$^+$ (J=1-0), CCH (J=1-0), SiO (J=2-1), HCN (J=2-1), HCO$^+$ (J=1-0), CH_3OH (2(1,1)-1(1,0)), CS (J=2-1), SO (J=3(2)-2(1)), $H_{40\alpha}$, and HC_3N (J=11-10) (see Table 2 in Liu et al. (2020c)). The spectral resolutions for SPWs 1-6 were ∼0.2-0.4 km s^{-1}, while SPWs 7 and 8 had a spectral resolution of ∼1.6 km s^{-1} (Liu et al. 2020c).

We also utilized Band 6 data from the Querying Underlying Mechanisms of Massive Star Formation with ALMA-Resolved Gas Kinematics and Structures (QUARKS; PIs: Lei Zhu, Guido Garay, and Tie Liu) project, which provides an angular resolution of ∼0.3 ″ and a maximum recoverable scale as large as ∼27 ″ (Liu et al. 2024; Xu et al. 2024). The QUARKS observations were conducted using the ACA and 12 m arrays (C43-2 and C43-5; Liu et al. 2024; Xu et al. 2024) and used four wide SPWs, each with a bandwidth of ∼1873 MHz. Each channel has a velocity resolution of ∼0.7 km s^{-1}, and the combined line sensitivity is ∼3 mJy beam^{-1} (Liu et al. 2024).

2.3. Spitzer and Herschel infrared data

The Galactic Legacy Infrared Mid-Plane Survey Extraordinaire (GLIMPSE) conducted observations in the mid-infrared wavelengths of 4.5 and 8 μm (Benjamin et al. 2003). The spatial resolutions of these two bands are 1.6 ″ and 1.9 ″, respectively (Fazio et al. 2004). Additionally, the 24 μm image data were obtained from the Multiband Infrared Photometer of the *Spitzer* MIPS Galactic Plane Survey (MIPSGAL; Carey et al. 2009). The resolution of the 24 μm image is 6 ″ (Rieke et al. 2004).

The *Herschel* key project Hi-GAL is an unbiased survey of the Galactic plane in the far-infrared wavelengths (Molinari et al. 2010b). It covers the entire Galactic plane within the nominal $|b| < 1°$ range. Observations were made using the Photodetector Array Camera and Spectrometer (PACS; Poglitsch et al. 2010) and Spectral and Photometric Imaging Receiver (SPIRE; Griffin et al. 2010) cameras on the *Herschel* space telescope, capturing continuum images at 70, 160, 250, 350, and 500 μm (Pilbratt et al. 2010). The spatial resolutions for these five bands are 5.8, 12.0, 18.2, 24.9, and 36.3 ″, respectively.

3. Results

3.1. High-resolution column density and temperature maps

Before deriving the H_2 column density and dust temperature from the *Herschel* images, several preprocessing steps were required. First, a few saturated pixels were present in the SPIRE 250 μm map of the G329 center region. Following the approach used by Lin et al. (2016) and Zhang et al. (2024b), we estimated the flux in the saturated areas via 2D Gaussian interpolation. Second, the PACS 70 and 160 μm images had not been corrected for zero-point offsets (Sadavoy et al. 2018). To recover the absolute intensity scale, the conventional method cross-calibrates PACS data with large-scale emission traced by Planck and IRAS observations, thereby performing a zero-point offset correction (Bernard et al. 2010). Specifically, we used *pacs_calibrate*[1] to convolve the PACS maps to the angular resolution of the Planck data, convert all maps to a common unit system and perform pixel-by-pixel comparisons (Tiwari et al. 2021; Karim et al. 2023). From the derived intensity differences, the zero-point offsets for the 70 and 160 μm images were determined to be 74.38 MJy sr^{-1} and 431.29 MJy sr^{-1}, respectively, and these corrections were applied to the original high-resolution PACS maps. This procedure effectively restores the absolute brightness level of the PACS images by compensating for the missing large-scale emission, thereby ensuring photometric consistency with the Planck and IRIS data. Third, we utilized the background subtraction method based on the Fourier transform, as proposed by Wang et al. (2015). The Fourier transform was performed on the original image to obtain high- and low-frequency components; the low-frequency components represented the background radiation and were subtracted from the data to remove the background from the *Herschel* images.

[1] https://github.com/ramseykarim/pacs_calibrate

To derive a high-resolution (18.2 ″) H_2 column density map, we employed the multi-scale decomposition technique introduced by Palmeirim et al. (2013). In this framework, the gas surface density (Σ) distribution smoothed to the SPIRE 250 μm resolution is expressed as the sum of three terms:

$$\Sigma_{250} = \Sigma_{500} + (\Sigma_{350} - \Sigma_{500}) + (\Sigma_{250} - \Sigma_{350}), \tag{1}$$

where Σ_{500}, Σ_{350}, and Σ_{250} represent the surface density distributions convolved with the SPIRE beams at 500 μm, 350 μm, and 250 μm, respectively.

The derivation proceeds in three steps:

1. Large-scale term (Σ_{500}). Using a modified blackbody radiation model:

$$I_\nu = B_\nu(T_{\rm dust})\kappa_\nu\Sigma, \tag{2}$$

where B_ν is the Planck function and the dust opacity per unit dust mass is (Hildebrand 1983):

$$\kappa_\nu = 0.1\left(\frac{\nu}{1000\,{\rm GHz}}\right)^\beta {\rm cm^2\,g^{-1}} = 0.1\left(\frac{300\,\mu{\rm m}}{\lambda}\right)^\beta {\rm cm^2\,g^{-1}}, \tag{3}$$

where the dust emissivity index β is fixed to 2 in the fitting. All images at 70, 160, 250, and 350 μm were convolved to a circular Gaussian beam with a full width at half maximum (FWHM) of 36.4 ″ using the kernels provided by Aniano et al. (2011) and regridded to the same pixel size. The 70 μm PACS data were included in the spectral energy distribution (SED) fitting in addition to the 160–500 μm bands because the central region of G329 hosts active massive star formation, where the dust temperature is elevated and significant emission arises at shorter wavelengths. Including the 70 μm band enables SED fitting to capture the contribution of warmer dust better, providing a more accurate estimate of both the dust temperature and the surface density in regions affected by strong stellar heating. We then performed pixel-by-pixel SED fitting for images ranging from 70 μm to 500 μm using *Python*, obtaining a low-resolution surface density map, $\overline{\Sigma}_{500}$, and a dust temperature map, $T_{\rm dust,500}$.
2. Intermediate-scale correction ($\Sigma_{350} - \Sigma_{500}$). A higher-resolution (350 μm) map, $\overline{\Sigma}_{350}$, is derived from a similar SED fit excluding the 500 μm data. The term ($\overline{\Sigma}_{350}$ - $\overline{\Sigma}_{350} \times G_{500\_350}$) recovers intermediate spatial frequencies absent at 500 μm, where G_{500_350} is a circular Gaussian with FWHM $\sqrt{36.3^2 - 24.9^2} \approx 26.4''$.
3. Smallest scales ($\Sigma_{250} - \Sigma_{350}$). Instead of deriving a color temperature map from the 160-250 μm intensity ratio as in previous HGBS works, we performed pixel-by-pixel SED fitting using the 70, 160, and 250 μm bands to simultaneously estimate the dust temperature and surface density at the SPIRE 250 μm resolution. This approach accounts for the contribution of warmer dust components traced by the 70 μm emission in the massive star-forming hub, providing a more accurate representation of the high-resolution column density and temperature structures. The resulting fine-scale component, ($\overline{\Sigma}_{250} - \overline{\Sigma}_{250} * G_{350\_250}$), where G_{350_250} is a circular Gaussian with a FWHM $\sqrt{24.9^2 - 18.2^2} \approx 17.0''$, preserves the small-scale information accessible only at wavelengths ≤ 250 μm.

Finally, by combining the above three terms of multi-scale information, high-resolution surface density and temperature

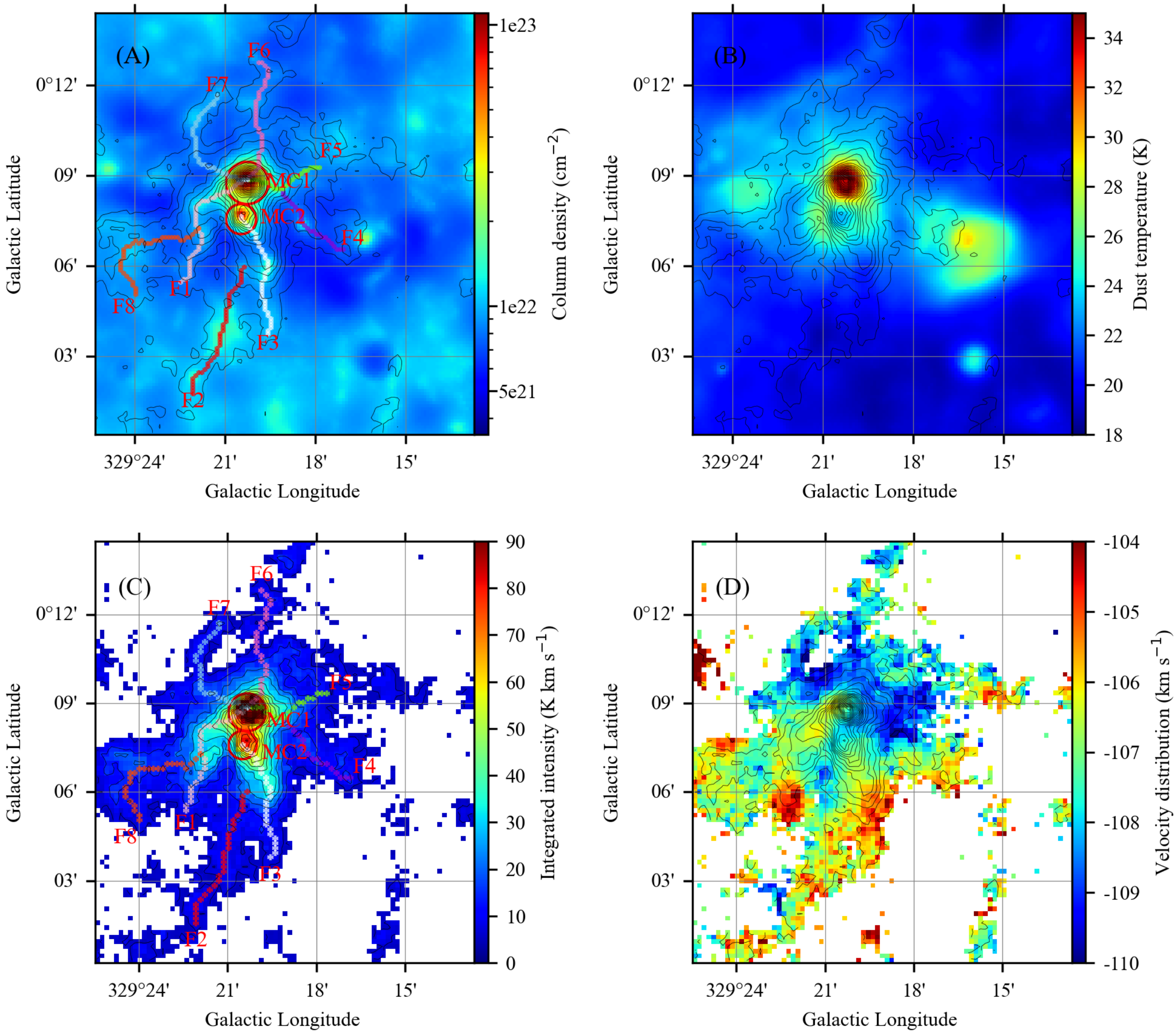

Fig. 2. Morphological structure of the G329 molecular cloud. *Panel A*: Distribution of hydrogen column density obtained from SED fitting. The colored plus (+) represents the spines of filaments corrected based on the ^{13}CO (J=2-1) velocity distribution. MC 1 and MC 2 are dense clumps identified in the 870 μm continuum (Urquhart et al. 2014, 2018). *Panel B*: Distribution of dust temperature. *Panel C*: Color map representing the distribution of the integrated intensity (moment 0) for ^{13}CO (J=2-1), with pixels below 5 σ level masked out. *Panel D*: Velocity distribution (moment 1) of ^{13}CO (J=2-1). In panels A, B, C, and D, the black contours represent the ^{13}CO (J=2-1) integrated intensity distribution, ranging from 4% to 100% of the peak column density in intervals of 4%.

maps were obtained (∼18.2″), as expressed by the following equation (Palmeirim et al. 2013):

$$\overline{\Sigma}_{250} = \overline{\Sigma}_{500} + (\overline{\Sigma}_{350} - \overline{\Sigma}_{350} \times G_{500\_350}) + (\overline{\Sigma}_{250} - \overline{\Sigma}_{250} * G_{350\_250}). \quad (4)$$

The surface density was converted into column density using $\overline{\Sigma}_{250} = \mu_{H_2} m_H N_{H_2}$, where $\mu_{H_2} = 2.8$ is the molecular weight per hydrogen molecule adopted from Kauffmann et al. (2008), m_H is the H-atom mass, and N_{H_2} is the H_2 column density. Panels A and B of Fig. 2 display the distributions of column density and dust temperature for the molecular cloud G329. The positions of higher column density correspond to MC 1 and MC 2, which were identified based on the 870 μm radiation by Urquhart et al. (2018) (see Fig. 2). From the dust temperature distribution, we observe that MC 1 is the hottest region within the molecular cloud (with an average temperature of 30.8 K). This suggests the possibility of intense star-forming activity within MC 1. In contrast, the average temperature of MC 2 is 24.7 K, significantly lower than that of MC 1, which is consistent with the fact that star formation activity in MC 2 is relatively weaker compared to MC 1 (see Fig. 1).

3.2. Hub-filament system in the G329 molecular cloud

To characterize the filaments within the G329 molecular cloud, we identified filamentary skeletons with *FilFinder*[2] (Koch &

[2] https://fil-finder.readthedocs.io/en/latest/

Rosolowsky 2015) on the hydrogen column density map (see Fig. A.1). The analysis was restricted to regions where the ^{13}CO (J=2-1) integrated intensity exceeds a threshold defined as 4% of the peak integrated intensity and simultaneously above the $3\,\sigma$ level. This combined criterion provides a conservative, physically motivated mask that suppresses unrelated foreground and background emission while retaining coherent molecular gas structures (see Panels C and D of Fig. 2). Prior to skeleton extraction, the column density map was preprocessed using the *FilFinder* flattening procedure (flatten_percent = 90) to suppress background variations and enhance the contrast of narrow filamentary structures. We note that *FilFinder* does not impose explicit thresholds on filament aspect ratio or density contrast. Instead, filament candidates were defined through skeletonization within the adopted mask and subsequent pruning based on minimum skeleton and branch lengths expressed in units of the beam size (5 and 3 beam widths, respectively, in the default *FilFinder* settings). The column-density skeletons were used as the initial morphological reference for defining the final filament spines after the velocity-coherence checks described below.

To perform these velocity-coherence checks, we compared the column-density skeletons with the ^{13}CO (J=2-1) integrated intensity distribution and channel maps (see Fig. A.2 and Table A.1) to confirm velocity continuity along each structure (Wang et al. 2015). Using these skeletons as a reference, minor manual adjustments were applied based on the velocity-channel information to ensure that the final filament spines follow coherent velocity structures, rather than relying solely on automated morphological extraction (additional details are provided in Appendix A). These refined spines are used throughout the paper for all subsequent kinematic and physical analyses.

The characteristic widths of the filaments were derived using *RadFil*[3] (Zucker & Chen 2018) in the hydrogen column density map, which constructs transverse profiles by performing perpendicular cuts along each filament spine and fits the averaged profiles with a Gaussian model after background subtraction. The widths, derived from the fitted FWHM, are summarized in Table 1. Filament elongation was quantified a posteriori using the aspect ratio, defined as the ratio of the filament length (measured from the longest spine path) to its FWHM width; these values are also listed in Table 1. Although the hydrogen column density map has a beam size of $\sim$18.2$''$, introducing uncertainty in the projected widths, this effect is negligible for mass estimates because most of the mass is concentrated near the filament crest. Panel A of Fig. 2 displays the spines of eight parsec-scale filaments and two massive clumps (MC 1 and MC 2). Filaments F 1, F 5, F 6, and F 7 converge toward MC 1, indicating that MC 1 is the dominant central clump within the hub region. F 3 converges toward MC 2. F 8, F 2, and F 4 are identified as sub-filaments connected to F 1, F 3, and F 5, respectively. This parsec-scale configuration provides the overall context for subsequent high-resolution observations of MC 1 within the hub region.

3.3. The physical properties of filaments and clumps

Based on the positions of the two clumps within the hub, MC 1 and MC 2, and their line-of-sight velocities, we used the *Parallax-based distance calculator V2*[4] to estimate the kinematic distance of the G329 molecular cloud, obtaining a value of 5.6 (±0.8) kpc (Reid et al. 2016, 2019). For comparison, Urquhart et al. (2018) reported distances of $\sim$7.2 kpc for MC 1 and MC 2, and the distance to a nearby star cluster is $\sim$6.0 kpc. The discrepancy arises partly because the calculator relies on the input line-of-sight velocity, and our measured peak velocity from C^{18}O (J=2-1) spectral line fitting (-107.5 km s^{-1}; see Fig. B.1) is slightly lower than the value of -107.1 km s^{-1} reported by Urquhart et al. (2018). Additionally, the latest version of the distance calculator utilizes an updated Galactic rotation model, which differs from previous versions and contributes to the discrepancy. Our distance estimate is consistent within uncertainties with that provided by Liu et al. (2024). Therefore, we adopt 5.6 (±0.8) kpc as the distance of G329 for all subsequent analysis of the HFS.

3.3.1. The physical properties of the filaments

First, we measured the lengths and derived the masses of the identified filaments. The filament masses were estimated by summing the hydrogen column density over all pixels within each filament:

$$M_{\mathrm{H_2}} = \mu_{\mathrm{H_2}} m_{\mathrm{H}} \sum_i A_{\mathrm{pixel}}(i) N_{\mathrm{H_2}}(i), \tag{5}$$

where $A_{\mathrm{pixel}}(i)$ is the area of a pixel and $N_{\mathrm{H_2}}(i)$ is the corresponding hydrogen column density. Table 1 summarizes the derived physical properties of the eight filaments within G329, with uncertainties propagated mainly from the distance errors and fitting errors. The estimated line masses (M/l) span from $\sim$118 (±40) to $\sim$520 (±174) M$_\odot$ pc^{-1}. Among them, the sub-filaments F 2, F 4, and F 8 exhibit relatively low line-mass densities. These values are comparable to those reported for other massive HFSs, for example, 125 - 439 M$_\odot$ pc^{-1} in G323.46-0.08 (Ma et al. 2023) and 167 - 620 M$_\odot$ pc^{-1} in G310.142+0.758 (Yang et al. 2023). The similarity suggests that the G329 HFS contains a substantial mass reservoir along its filaments in the vicinity of the central hub region. Although the ^{13}CO (J=2-1) spectra along these structures generally exhibit a single dominant velocity component (see Sect. 3.3.2), the available single-dish data ($\sim$30$''$, corresponding to $\approx$0.8 pc at 5.6 kpc) lack sufficient resolution to reveal finer internal structures within the filaments. Moreover, both the ^{13}CO and *Herschel* observations indicate that the filaments in G329 are relatively diffuse ($A_V < 7$), suggesting that their unresolved interiors are unlikely to harbor dense, self-gravitating substructures. Consequently, the line mass values reflect the average mass distribution of diffuse, non-self-gravitating gas, rather than the mass distribution of true dense filaments. Since the hydrostatic, isothermal cylindrical assumption underlying the virial line mass (Ostriker 1964) is physically meaningful only for gravity-dominated filaments (Inutsuka & Miyama 1997; Fiege & Pudritz 2000; André et al. 2014), comparing such beam-averaged line masses with critical or virial thresholds would be misleading. We therefore present the derived filament line masses merely as beam-averaged estimates that describe the parsec-scale gas distribution, without interpreting them as indicators of intrinsic stability.

3.3.2. Velocity components and velocity dispersion of the filaments

As shown in Fig. B.2, we extracted the averaged ^{13}CO (J=2-1) spectra at multiple positions along each filament. All spectra exhibit a single velocity component, indicating that the parsec-scale gas motion within the G329 molecular cloud is relatively coherent. The total velocity dispersions (σ_{tot}) of the eight filaments range from 0.50±0.07 to 1.39±0.06 km s^{-1} (see Table 1).

[3] `https://github.com/catherinezucker/radfil`
[4] `http://bessel.vlbi-astrometry.org/node/378`

Table 1. Physical parameters of the filaments.

Source ID	l	FWHM$^{(a)}$	Aspect ratio$^{(b)}$	M_{H_2}	$T_{dust}^{(c)}$	M/l	σ_{tot}	$\nabla V_{\parallel}^{(d)}$	$\lvert\dot{M}_{\parallel}\rvert$
	(pc)	(pc)	(-)	($M_\odot$)	(K)	($M_\odot$ pc^{-1})	(km s^{-1})	(km s^{-1} pc^{-1})	($M_\odot$ year^{-1})
F 1	8.2 (±1.2)	1.2 (±0.2)	6.6 (±1.4)	3092 (±924)	24.0	378 (±126)	1.39 (±0.06)	0.29	$9.18\,(\pm2.74)\times10^{-4}$
F 2	8.1 (±1.2)	1.3 (±0.2)	6.5 (±1.4)	2094 (±626)	19.7	258 (±86)	0.50 (±0.07)	0.10	$2.24\,(\pm0.67)\times10^{-4}$
F 3	7.4 (±1.1)	1.3 (±0.2)	5.9 (±1.2)	2870 (±858)	21.4	388 (±130)	1.30 (±0.06)	0.22	$6.54\,(\pm1.95)\times10^{-4}$
F 4	5.2 (±0.8)	0.8 (±0.1)	6.2 (±1.3)	612 (±183)	23.4	118 (±40)	0.92 (±0.04)	0.82	$5.14\,(\pm1.54)\times10^{-4}$
F 5	4.6 (±0.7)	1.1 (±0.2)	4.2 (±0.9)	2393 (±715)	25.3	520 (±174)	1.29 (±0.06)	-0.39	$9.57\,(\pm2.86)\times10^{-4}$
F 6	7.4 (±1.1)	1.2 (±0.2)	6.0 (±1.3)	2447 (±731)	23.8	330 (±110)	1.03 (±0.04)	0.01	$3.48\,(\pm1.04)\times10^{-5}$
F 7	7.4 (±1.1)	1.1 (±0.2)	6.5 (±1.4)	2801 (±837)	24.5	379 (±127)	0.90 (±0.06)	-0.16	$4.61\,(\pm1.38)\times10^{-4}$
F 8	7.8 (±1.2)	1.9 (±0.3)	4.2 (±0.9)	2443 (±730)	21.5	312 (±104)	0.88 (±0.06)	-0.09	$2.28\,(\pm0.68)\times10^{-4}$

Notes. The filaments listed in this table are identified at lower angular resolutions and are not assumed to have a one-to-one correspondence with the intra-hub filaments resolved by ALMA.
$^{(a)}$ The width of the filaments is defined as the mean FWHM derived from radial Gaussian fitting to the H_2 column density profiles.
$^{(b)}$ Aspect ratio, defined as the ratio between the filament length and its FWHM width.
$^{(c)}$ The average value of dust temperature on the filaments.
$^{(d)}$ Velocity gradient adopted for the mass accretion rate calculation. The values are taken from the velocity gradients along the filaments listed in Table C.1.

In the hub, particularly within MC 1, the gas shows significantly broader lines (e.g., 3.2 km s^{-1} at the position H1, defined as the MC 1 center), compared to the narrower profiles observed in MC 2 (e.g., 1.8 km s^{-1} at the position H2, defined as the MC 2 center; see Table B.1). The larger molecular line widths observed in MC 1 are consistent with previous studies, which suggest the presence of enhanced turbulence or feedback-driven motions in the vicinity of massive star-forming regions.

In general, the gas in the hub tends to exhibit broader lines (Treviño-Morales et al. 2019; Ma et al. 2023), consistent with our observations. Along most filaments, the velocity dispersion decreases progressively outward from the hub. For instance, along F 5, the velocity dispersion decreases from 3.2 km s^{-1} at H1 (the MC 1 center) to 1.4 and 0.9 km s^{-1} at F5a (closer to the hub) and F5b (far from the hub), respectively. Similarly, along F 6, it declines from 3.2 km s^{-1} at H1 (the MC 1 center) to 1.6 and 0.8 km s^{-1} at F6a (closer to the hub) and F6b (far from the hub), respectively (additional details can be seen in Appendix B and Table B.1). This systematic decrease suggests that the enhanced velocity dispersion near the hub likely originates from active gas motions and strong stellar feedback, while the outer filaments trace more quiescent, diffuse gas.

3.3.3. Gas velocity gradient and mass accretion rate along the filaments

In HFSs, filaments have often been interpreted as conduits that channel material toward central hubs and may facilitate the formation of massive stars (Myers 2009; Peretto et al. 2013; Kumar et al. 2020). For G329, we therefore examined whether the projected velocity distribution along the filaments is consistent with organized motions toward the hub. Clear velocity gradients along the filaments can be identified, suggesting possible systematic gas motion on parsec scales (see Appendix C).

Among the eight filaments, F 1, F 2, F 3, F 4, and F 5 exhibit relatively consistent and nearly linear velocity gradients along their main spines. In contrast, the gas velocity distributions along F 6, F 7, and F 8 show significant fluctuations and deviate from the linear fits. The fitted linear velocity gradients for F 1, F 2, F 3, F 4, and F 5 are 0.29, 0.10, 0.22, 0.82, and -0.39 km s^{-1} pc^{-1}, respectively (see Figs. C.1, C.2, C.3, and C.4). In several cases the absolute gradients measured over the inner portions of the spines are larger than those measured farther from the hub; for example, within 1.7 pc from the relevant reference clump, F 1 shows a gradient of 0.78 km s^{-1} pc^{-1}, while F 5 and F 6 exhibit gradients of -0.81 and -0.87 km s^{-1} pc^{-1}, respectively (see Figs. C.1, C.4, and C.5). We emphasize that these projected gradients are not determined solely by the distance to the hub. They also depend on the inclination angle of the system, the adopted reference clump (MC 1 or MC 2), and the points chosen along the spine to measure the velocity gradients.

To quantify the possible mass transfer associated with these projected motions, we estimated the mass accretion rate along each filament using the standard cylindrical estimate commonly adopted in filament studies (e.g., Kirk et al. 2013):

$$\dot{M}_{\parallel} = \frac{\nabla V_{\parallel} M}{\tan\theta}, \tag{6}$$

where $\nabla V_{\parallel}$ is the projected velocity gradient along the filament obtained from a linear fit, M is the total filament mass, and θ is the inclination angle of the filament to the plane of the sky (assumed to be 45 °). The resulting mass accretion rates toward the hub range from 3.48×10^{-5} to $9.57\times10^{-4}\,M_\odot\,yr^{-1}$, with a median value of $\sim4.88\times10^{-4}\,M_\odot\,yr^{-1}$ (see Table 1).

We note that the observed filaments are relatively broad at the current spatial resolution, and their internal substructures remain unresolved. Consequently, the velocity gradients and mass accretion rates estimated here trace average projected motions of the diffuse molecular gas along the filaments and should be regarded as order-of-magnitude indicators rather than precise measurements of the detailed kinematics of internal, finer-scale structures. Unresolved substructures, variations in filament density, core formation, or feedback processes may further introduce deviations from the linear velocity fits (Maity et al. 2025). Despite these limitations, the hydrogen column density increases near the hub region in several filaments (see Figs. C.1, C.2, C.4, C.5, and C.6), and we used this location to define the hub edge (see Appendix C). The dust temperature also increases along several filaments toward MC 1 (see Table C.1). For F 1, F 5, F 6, and F 7, the velocity, column-density, and dust-temperature gradients measured in the inner portions of the filaments are larger than those measured farther from the hub region (see Figs. C.1, C.4, C.5, and C.6; see also Table C.1). We caution that these inner-outer differences should be interpreted as qualitative tendencies, not as evidence for a strictly monotonic dependence on distance from the hub. Nevertheless, the increase in column den-

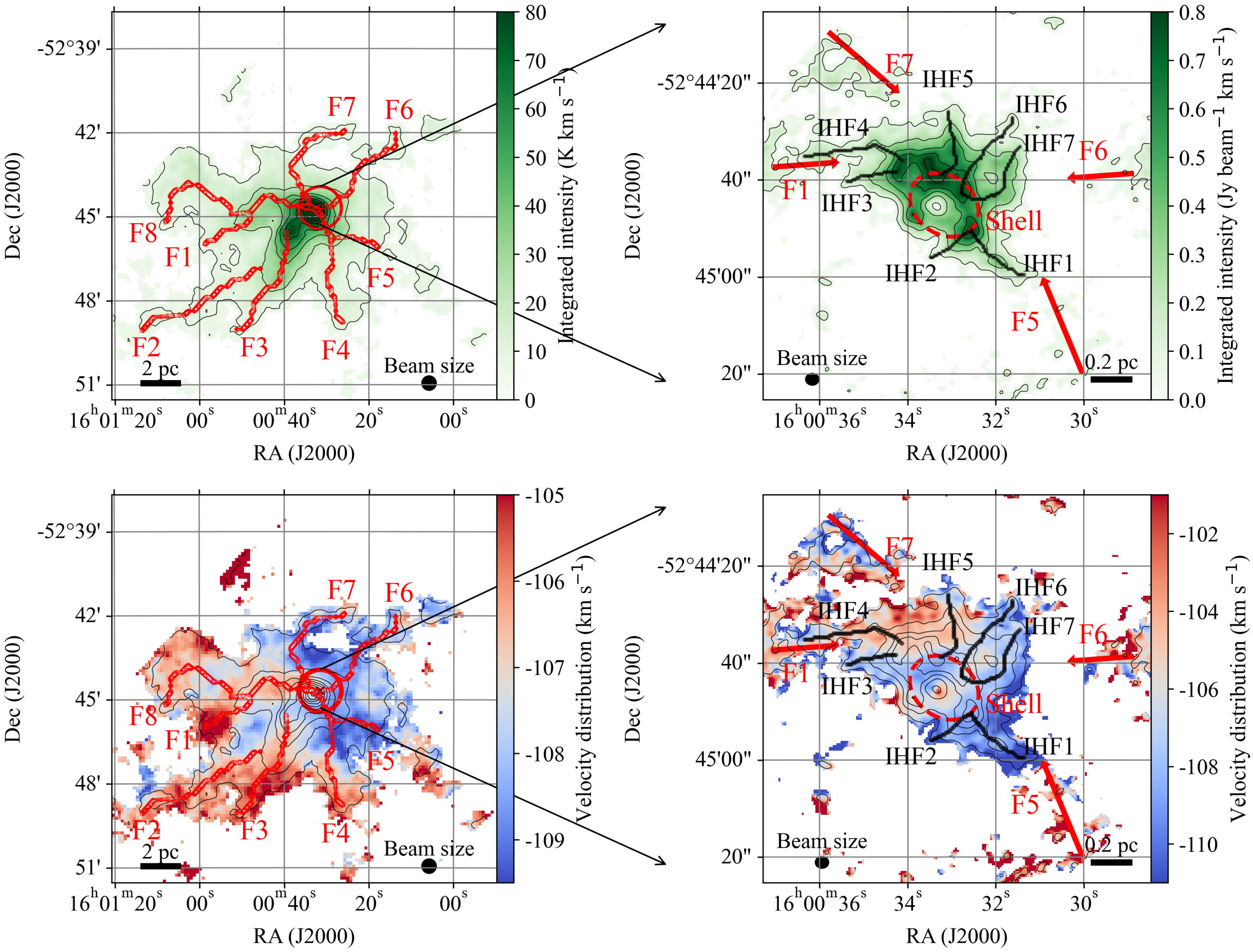

Fig. 3. Distribution of filamentary structures and gas kinematics in the G329 molecular cloud. *Left panels*: Integrated intensity (moment 0; top) and velocity field (moment 1; bottom) of ^{13}CO (J=2-1) in G329. The red curves (F 1-F 8) mark the spines of the filaments identified at lower angular resolutions. The black contours represent the integrated intensity values of ^{13}CO (J=2-1), ranging from 5% to 95% of the peak value in 10% steps. *Right panels*: Zoomed-in views of MC 1 observed by the ATOMS project. Top: Integrated intensity (moment 0) map of $H^{13}CO^+$ (J=1-0). Bottom: Its velocity field (moment 1). The dashed black curves (IHF 1-IHF 7) indicate the spines of the intra-hub filaments identified from the $H^{13}CO^+$ (J=1-0) integrated intensity map using *FilFinder*. The red curve outlines the shell-like structure. The black contours show the integrated intensity of $H^{13}CO^+$ (J=1-0), from 10% to 90% of the peak value in 20% steps. The overlaid red arrows indicate approximate projected convergence directions inferred from the sky-plane orientations of the filaments and the observed velocity distribution. These arrows are intended to guide the comparison of the two velocity fields; they neither imply a one-to-one morphological correspondence nor a uniquely determined inflow geometry.

sity toward the hub region indicates that substantial gas is concentrated in the central region relative to the surrounding filaments.

3.3.4. The physical properties of clumps MC 1 and MC 2

The morphological structure of the G329 molecular cloud shows that MC 1 and MC 2 are two massive clumps embedded in the same HFS hub rather than two independent hubs (see Fig. 2). In this morphological sense, they can be treated as two dense hub nodes with different evolutionary states, consistent with the filaments-to-clusters picture in which hubs can contain multiple dense nodes (Kumar et al. 2020, 2022, 2025). As discussed in Sect. 1 and 3.1, the gas in MC 1 is denser and has higher dust temperatures. Table 2 presents the physical properties of two clumps. MC 1 and MC 2 have masses of ∼4210 (±1259) and ∼1483 (±443) $M_\odot$, respectively, classifying them as massive clumps. The surface density of the clumps is calculated from the expression (cf. Colombo et al. (2019)):

$$\Sigma = \frac{M}{\pi R_{\rm eq}^2}, \tag{7}$$

where the M represents the mass of the clump and $R_{\rm eq}$ is the equivalent radius of the clump (Rigby et al. 2019). The surface densities of MC 1 and MC 2 are ∼0.19 (±0.08) and ∼0.12 (±0.05) g cm^{-2}, with both exceeding 0.05 g cm^{-2}. This suggests the potential for high-mass star formation (He et al. 2015). We also examined the mass-radius relationship ($M(r) > 580\,M_\odot\,(R_{\rm eq}\,{\rm pc}^{-1})^{1.33}$; Kauffmann & Pillai 2010) for MC 1 and MC 2 and found that both are consistent with the formation of high-mass stars. These pieces of evidence collectively suggest that the current MC 1 and MC 2 continue to serve as sites for the ongoing formation of massive stars. The average hydrogen number density of each clump was computed from the expression:

$$\overline{n}(H_2) = \frac{3}{4\pi}\frac{M}{\mu_{\rm H_2} m_{\rm H} {R_{\rm eq}}^3}, \tag{8}$$

Table 2. Physical parameters of clumps.

Clump	l_c	b_c	R_{eq} $^{(a)}$	T_{dust} $^{(b)}$	$M^{(c)}$	$\Sigma^{(d)}$	α_{vir} $^{(e)}$
-	(°)	(°)	(pc)	(K)	($M_\odot$)	(g cm^{-2})	-
MC 1	329.34	0.15	1.23 (±0.18)	30.8	4210 (±1259)	0.19 (±0.08)	1.74 (±0.35)
MC 2	329.34	0.13	0.89 (±0.13)	24.7	1483 (±443)	0.12 (±0.05)	1.95 (±0.45)

Notes. $^{(a)}$ The equivalent radius of the clump, $R_{eq} = (\frac{A_{clump}}{\pi})^{\frac{1}{2}}$ (cf. Rigby et al. (2019)).
$^{(b)}$ Average dust temperatures of the clump.
$^{(c)}$ Clump mass calculated from the values from the hydrogen column density map.
$^{(d)}$ Clump surface densities.
$^{(e)}$ Clump virial parameters.

The average hydrogen number densities of MC 1 and MC 2 are 7.8 (±2.3) and 7.3 (±2.2) $\times 10^3$ cm^{-3}, respectively. The virial parameter (α_{vir}) is commonly used to assess the dynamic state of clumps as follows:

$$\alpha_{vir} = \frac{5\sigma_\mu^2 R_{eq}}{GM}, \quad (9)$$

where G is the gravitational constant and σ_μ is the $C^{18}O$ (J=2-1) velocity dispersion of the clumps. The σ_μ values for MC 1 and MC 2 are 2.26 and 1.67 km s^{-1}, respectively (as seen in Fig. B.1). The range $1 < \alpha_{vir} < 2$ signifies equilibrium between kinetic and gravitational energies; $\alpha_{vir} < 1$ indicates collapse under gravity; and $\alpha_{vir} > 2$ implies dissipation due to dominant kinetic energy (MacLaren et al. 1988; Urquhart et al. 2018). The virial parameters for MC 1 and MC 2 are 1.74 (±0.35) and 1.95 (±0.45), respectively, placing both clumps within the range typically expected for gravitationally bound systems. The relatively high velocity dispersions in MC 1 and MC 2 may be partly attributed to the infall of surrounding gas. Moreover, in the case of MC 1, they may also be attributed to stellar feedback and outflows driven by embedded massive stars, as indicated by the prominent line wing broadening in the averaged ^{13}CO (J=2-1) spectrum (see Fig.B.1). Nevertheless, owing to their large masses, the gravitational binding of the clumps is sufficient to counterbalance these effects, maintaining them in a state of virial equilibrium. Compared with MC 1, MC 2 exhibits a lower luminosity-to-mass ratio, weaker infrared emission (see Sect. 1), and lower temperatures and velocity dispersion (see Table 2 and Fig.B.1), indicating that it has not yet developed significant star formation activity.

3.4. Observations of MC 1 with high-resolution data from ALMA

3.4.1. Intra-hub filaments in MC 1

The $H^{13}CO^+$ (J=1-0) line emission is typically optically thin, making it a reliable probe of dense gas kinematics and dynamics (Liu et al. 2020c,b; Yang et al. 2023). Its spatial distribution generally follows that of dense gas revealed by *Herschel* observations (Shimajiri et al. 2017). Therefore, using $H^{13}CO^+$ (J=1-0) emission to trace dense filamentary structures is reasonable (Li et al. 2022; Xu et al. 2023; Yang et al. 2023).

In this study, we used *FilFinder* (Koch & Rosolowsky 2015) to extract elongated filamentary structures from the $H^{13}CO^+$ (J=1-0) integrated intensity map, identifying seven intra-hub filaments (IHFs). These IHFs trace the short, dense filamentary network inside MC 1 and are used as the structural basis for the high-resolution kinematic analysis below.

As shown in the left panels of Fig. 3, the ^{13}CO (J=2-1) data show a clear parsec-scale velocity segregation across the G329 molecular cloud, with predominantly blueshifted gas on one side of MC 1 and redshifted gas on the other. At higher angular resolution, the $H^{13}CO^+$ (J=1-0) emission tracing the dense gas within MC 1 shows a similar velocity structure, with blue- and redshifted components distributed across the IHFs. Comparable velocity signatures are also observed in HC_3N (J=11-10), HCN (J=1-0), $H^{13}CN$ (J=1-0), and CS (J=2-1) (see Fig. D.1), indicating that the dense gas within MC 1 shares a common kinematic framework across multiple tracers.

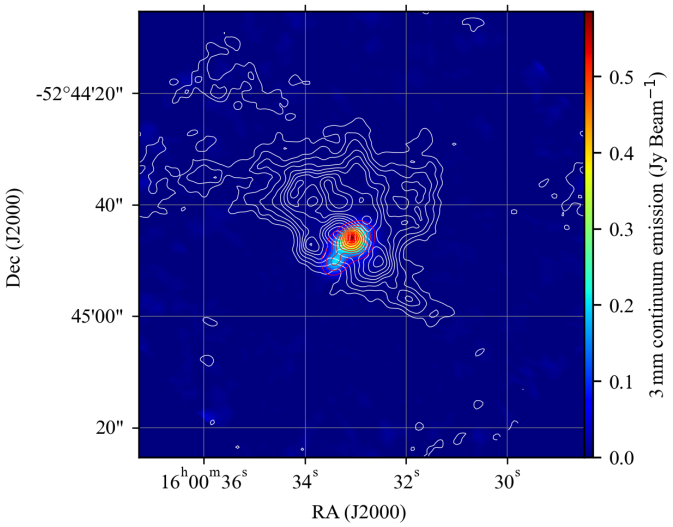

Fig. 4. Color map representing the radiation intensity at 3 mm continuum radiation. The white contour represents the intensity distribution of $H^{13}CO^+$ (J=1-0). The contour lines range from 10% to 100% of the peak intensity in 10% peak intensity intervals. The red contour lines represent the intensity distributions of the $H_{40\alpha}$ emission, respectively, ranging from 10% to 100% of the peak intensity in 10% peak intensity intervals.

3.4.2. The ultracompact H II region at the center of MC 1

In ALMA Band 3, $H^{13}CO^+$ (J=1-0), along with several other molecular tracers (e.g., CS and HCN), reveals an ionized cavity at the center of MC 1. The intensity distributions of the 3 mm continuum thermal emission and the $H_{40\alpha}$ radio recombination line are largely consistent with each other and fill the interior of this cavity (see Fig. 4). It is worth noting that the peak positions of the 3 mm continuum emission and the $H_{40\alpha}$ radio recombination line do not exactly coincide with the center of the cavity traced by molecular lines, which may be caused by projection effects. Molecular line observations in MC 1 trace an elliptical ring structure surrounding the cavity (including lines such as $H^{13}CO^+$ (J=1-0), as shown in the right panels of Fig. 3). Together, these observations suggest that massive star formation is taking place at the center of MC 1. Strong feedback from the central star cluster has likely swept up the surrounding gas into a shell, creating a bubble structure. Such shells, compressed and shaped by the expanding H II region, can promote the formation of massive dense structures that may in turn host the birth of massive stars (Zhang et al. 2024a).

Table 3. Physical parameters of the intra-hub filaments.

Source ID	l (pc)	FWHM$^{(a)}$ (pc)	M_{H_2} ($M_\odot$)	M/l ($M_\odot$ pc^{-1})	$(M/l)_{\rm line,vir}$ ($M_\odot$ pc^{-1})	$\sigma^{(b)}$ (km s^{-1})	$\nabla V_{\parallel}{}^{(c)}$ (km s^{-1} pc^{-1})	$\lvert\dot{M}_{\parallel}\rvert$ ($M_\odot$ year^{-1})
IHF 1	0.52 (±0.08)	0.16 (±0.02)	308 (±92)	589 (±197)	905 (±103)	1.40 (±0.08)	-4.89	$1.54\,(\pm0.46)\times10^{-3}$
IHF 2	0.29 (±0.04)	0.07 (±0.01)	190 (±57)	649 (±217)	1297 (±139)	1.67 (±0.09)	4.02	$7.79\,(\pm2.33)\times10^{-4}$
IHF 3	0.31 (±0.05)	0.15 (±0.02)	156 (±47)	494 (±165)	1453 (±365)	1.77 (±0.22)	3.21	$5.11\,(\pm1.53)\times10^{-4}$
IHF 4	0.61 (±0.09)	0.15 (±0.02)	242 (±72)	398 (±133)	362 (±39)	0.88 (±0.05)	-1.77	$4.37\,(\pm1.31)\times10^{-4}$
IHF 5	0.42 (±0.06)	0.15 (±0.02)	425 (±127)	1007 (±337)	2040 (±172)	2.09 (±0.09)	4.97	$2.16\,(\pm0.65)\times10^{-3}$
IHF 6	0.57 (±0.08)	0.17 (±0.03)	411 (±123)	723 (±242)	1521 (±252)	1.81 (±0.15)	2.11	$8.87\,(\pm2.65)\times10^{-4}$
IHF 7	0.55 (±0.08)	0.15 (±0.02)	454 (±136)	832 (±278)	1298 (±128)	1.67 (±0.08)	1.90	$8.81\,(\pm2.63)\times10^{-4}$

Notes. The intra-hub filaments listed in this table are identified in MC 1 at ALMA resolutions and are not direct geometric extensions of the filaments listed in Table 1.
$^{(a)}$ The width of the intra-hub filaments was obtained by performing a radial Gaussian fit to the $H^{13}CO^+$ (J=1-0) integrated intensity, resulting in the average FWHM.
$^{(b)}$ The velocity dispersion (FWHM/$\sqrt{8\ln 2}$) of intra-hub filaments, calculated from $H^{13}CO^+$ (J=1-0).
$^{(c)}$ The velocity gradient, $\nabla V_{\parallel}$, measured along the projected spine of each intra-hub filament, using the same method adopted for the filaments listed in Table 1.

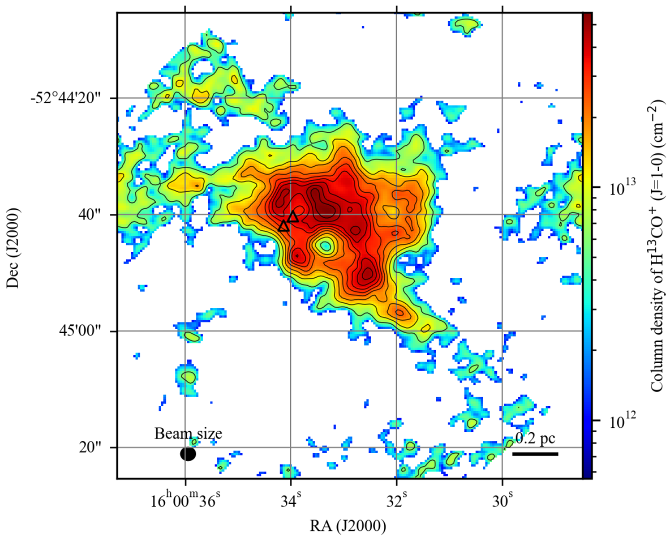

Fig. 5. Column density distribution of $H^{13}CO^+$ (J=1-0) in MC 1. The black contours indicate the $H^{13}CO^+$ (J=1-0) column density levels, ranging from 10% to 100% of the peak value in 10% steps. The black triangles mark the positions of the outflow-driving sources presented in Appendix F.

3.4.3. The column density of $H^{13}CO^+$ (J=1-0) in MC 1

We employed a standard procedure to estimate the mass based on the emission of $H^{13}CO^+$ (J=1-0). First, the column density for a linear, rigid rotor in the optically thin regime, assuming a filling factor of unity, was calculated using the expression (Garden et al. 1991):

$$N_{ij} = \frac{3k_B}{8\pi^3 B_{\rm rot}\mu^2}\frac{(T_{{\rm ex},ij} + hB_{\rm rot}/3k_{\rm B})}{(J+1)}\frac{\exp(E_J/k_{\rm B}T_{{\rm ex},ij})}{[1-\exp(-h\nu/k_{\rm B}T_{{\rm ex},ij})]} \times \frac{1}{[J(T_{{\rm ex},ij}) - J(T_{\rm bg})]}\int T_{{\rm mb},ij}\,dv, \tag{10}$$

where $k_{\rm B}$ is the Boltzmann constant, h is the Planck constant, ν is the transition frequency (86.754288 GHz), μ is the permanent dipole moment of the molecule (3.89 Debye), J is the rotational quantum number of the lower state, $E_J = hB_{\rm rot}J(J+1)$ is the energy in the level J, $B_{\rm rot}$ is the rotational constant of the molecule (43.377302 GHz), $T_{{\rm mb},ij}$ is the brightness temperature of $H^{13}CO^+$ (J=1-0) at Pixel (i, j), and $T_{\rm bg}$ = 2.73 K is the cosmic background radiation temperature (Mather et al. 1994). The value $J(T)$ is defined as

$$J(T) = \frac{h\nu}{k_{\rm B}}\left(\frac{1}{e^{h\nu/k_{\rm B}T}-1}\right), \tag{11}$$

and the $T_{{\rm ex},ij}$ is excitation temperature at Pixel (i, j). We assumed local thermodynamic equilibrium (LTE), and therefore the main beam brightness temperature $T_{\rm mb}$ was derived from

$$T_{\rm mb} = f\left[J(T_{\rm ex}) - J(T_{\rm bg})\right](1-e^{-\tau}). \tag{12}$$

The beam filling factor, f, was taken to be 1 since ALMA can well resolve the structure (Xu et al. 2023). We assumed that $H^{13}CO^+$ (J=1-0) is optically thin, with $\tau \ll 1$. So, the Eq. (12) can simplify as $T_{\rm mb} = \tau\left[J(T_{\rm ex}) - J(T_{\rm bg})\right]$, and the $H^{13}CO^+$ (J=1-0) optical depth $\tau(H^{13}CO^+)$ is

$$\tau = \frac{T_{{\rm mb},ij}}{[J(T_{{\rm ex},ij}) - J(T_{\rm bg})]}, \tag{13}$$

where $T_{{\rm mb},ij}$ is approximately taken as the peak temperature on each pixel of $H^{13}CO^+$ (J=1-0). Assuming $T_{{\rm ex},ij}$ is approximately equal to the $T_{\rm dust}$, the $T_{{\rm ex},ij}$ in MC 1 was fixed at 31 K (see Table 2). By substituting this value into Eqs. (10) and (13), the column density distribution of $H^{13}CO^+$ (J=1-0) was obtained (see Fig. 5).

3.4.4. The physical properties of intra-hub filaments in MC 1

In Sect. 3.4.3, we obtained the column density distribution of $H^{13}CO^+$ (J=1-0) in MC 1. To calculate the mass, we converted the column density of $H^{13}CO^+$ (J=1-0) to hydrogen column density based on the abundance ratio between hydrogen molecules and $H^{13}CO^+$ (J=1-0), $X_{H^{13}CO^+} = [H^{13}CO^+/H_2]$. Based on some previous studies, empirical values for $X_{H^{13}CO^+}$ were taken as 1.3×10^{-10} (Hoq et al. 2013), 5×10^{-11} (Peretto et al. 2013), 9×10^{-12} (Liu et al. 2020a), 5.4×10^{-11} (Li et al. 2022), and $5(\pm3)\times10^{-11}$ (Xu et al. 2023), respectively. In this work, we adopted the mean of these empirical results, i.e., $X_{H^{13}CO^+}$ =

6×10^{-11}. The converted hydrogen column density has a maximum value of approximately 9.4×10^{23} cm^{-2}. The column density was then converted into mass using the equation from Xu et al. (2023)

$$M_{\mathrm{H_2}} = (X_{\mathrm{H^{13}CO^+}})^{-1} m_{\mathrm{H_2}} A D^2 \sum_{i,j}^{\mathrm{filament}} N_{ij}(\mathrm{H^{13}CO^+}), \quad (14)$$

where A is the angular area of a pixel, $D = 5.6$ kpc is the kinematic distance (see Sect. 3.3), and $m_{\mathrm{H_2}}$ is the mass of a hydrogen molecule.

Referring to the analysis in Sect. 3.3, we provided the physical properties of IHFs within MC 1. As shown in Table 3, the length range of the seven IHFs is 0.29 (±0.04) - 0.61 (±0.09) pc. The mass range is 156 (±47) - 454 (±136) $M_\odot$. The line mass range is 398 (±133) to 1007 (±337) $M_\odot$ pc^{-1}. The absolute range of gas velocity gradients for IHFs is 1.77 - 4.97 km s^{-1} pc^{-1} (see Fig. E.1). The absolute range of mass accretion rates is 0.44 (±0.13) - 2.16 (±0.65) × 10^{-3} $M_\odot$ year^{-1}, with the median value of about 8.81 (±2.63) × 10^{-4} $M_\odot$ year^{-1}. Considering simplifying the filament as an isothermal cylindrical gas structure, the stability of the filament was maintained by the interplay of gravitational forces and turbulent pressure, and the virial line mass of the filament was defined as (Chandrasekhar 1951; Wang et al. 2011; Treviño-Morales et al. 2019; Bhadari et al. 2020; Hacar et al. 2023):

$$(M/l)_{\mathrm{line,vir}} = \frac{2\sigma_{\mathrm{tot}}^2}{G} = 465 \left(\frac{\sigma_{\mathrm{tot}}}{1\,\mathrm{km\,s^{-1}}}\right)^2 \mathrm{M_\odot\,pc^{-1}}, \quad (15)$$

where σ_{tot} represents the total velocity dispersion in the filament, estimated using $H^{13}CO^+$ (J=1-0). When the line mass of a filament exceeds the virial line mass, it indicates that self-gravity can overcome internal pressure, and the filament undergoes fragmentation due to gravitational instability (Wang et al. 2014). The line masses of the IHFs, except for filament IHF 4, are all lower than their corresponding virial line masses. The relatively high virial line masses may be linked to ongoing gas inflow along the IHFs, consistent with the projected inward motions observed in MC 1 (see Fig. 3).

4. Discussion

4.1. Morphological relation between parsec-scale filaments and intra-hub filaments

A key question in this work is how the filaments identified at lower angular resolution relate to the IHFs resolved by ALMA within MC 1. Because of the large angular resolution gap, the spatial filtering of extended emission inherent to interferometric observations, and the attenuation of the ALMA primary-beam response toward the field edges, we did not attempt to establish a one-to-one morphological correspondence between individual parsec-scale filaments and specific IHFs. In particular, any apparent alignment between a given filament and an IHF in Fig. 3 should be interpreted as reflecting the projected convergence of structures toward the hub, rather than a direct geometric continuation of a single structure between the two angular resolutions considered in this work.

Morphologically, the G329 molecular cloud is organized into several parsec-scale filaments that converge toward a dense central hub region. At the angular resolution of the lower-resolution data, this central region appears as two compact clumps, MC 1 and MC 2, which can be regarded as two nodes within the same hub. The ALMA observations further show that the dense gas inside MC 1 is organized into a network of shorter and denser IHFs. In this respect, G329 resembles systems such as Mon R2, where the hub is better described as a compact filamentary network than as a single homogenous clump (Kumar et al. 2022). In Mon R2, higher-sensitivity *Herschel* column density analysis further reveals cascades of lower-density filaments coalescing into higher-density filaments and a compact network of short, dense filaments inside the hub (Kumar et al. 2022). For G329, the present data support a similar hub-as-a-network picture. However, because G329 is more distant and the available observations have a large angular resolution gap between the single-dish and ALMA data, we cannot directly trace the parsec-scale filaments into the hub or establish filament coalescence morphologically. The parsec-scale filaments may therefore correspond to unresolved groups of lower-density filaments that merge or reorganize toward the hub, but this interpretation remains qualitative.

4.2. Kinematic correspondence between parsec-scale filaments and intra-hub filaments

Although strict morphological continuity cannot be established, the velocity field on the two scales shows a similar global organization. On parsec scales, the ^{13}CO (J=2-1) data show a clear velocity pattern in the G329 HFS: filaments F 5, F 6, and F 7 are predominantly blueshifted along the line of sight, whereas F 1, F 2, F 3, F 4, and F 8 are predominantly redshifted (Fig. 2). Within MC 1, the dense gas traced by $H^{13}CO^+$ (J=1-0) and other high-density tracers exhibits a similar parsec-scale velocity pattern, with blueshifted emission on one side and redshifted emission on the other (Fig. 3; see also Fig. D.1). Although individual filament crests cannot be geometrically traced from cloud scales into the hub, the similarity of the velocity distribution indicates that the IHFs likely represent the dense sub-parsec scale expression of the parsec-scale velocity organization.

Position–velocity (P–V) diagrams show that systematic velocity gradients are present both along the parsec-scale filaments and within the IHFs, while the gradients measured in the IHFs are generally steeper (see Appendices C and E). Together with the similar velocity segregation seen on the two scales, this result suggests a scale-dependent change in the velocity field from the parsec-scale filaments to the denser structures in the hub interior.

From this perspective, the G329 results are broadly consistent with the hub-filament picture inferred in nearby, better-resolved systems. In Mon R2, the main filaments extend into the hub and their velocity gradients increase toward the hub, suggesting gas acceleration into the central region (Treviño-Morales et al. 2019). In the Orion ISF, relatively smooth gradients along the filament give way to accelerated motions toward the OMC-1 region (Hacar et al. 2017). G329 shows a similar qualitative tendency for steeper projected gradients toward the denser inner hub region traced by MC 1, and the similar red-blue velocity organization on the two scales suggests that the dense gas within MC 1 is broadly related to the global velocity organization of the surrounding parsec-scale filaments. Taken together with the morphological comparison discussed above, these kinematic similarities suggest that G329 may represent a more distant and less well-resolved analog of nearby HFSs, such as Mon R2 and Orion, with the apparent differences arising at least partly from distance and angular resolution limitations rather than from a fundamentally different physical configuration. Nevertheless, this interpretation should remain qualitative

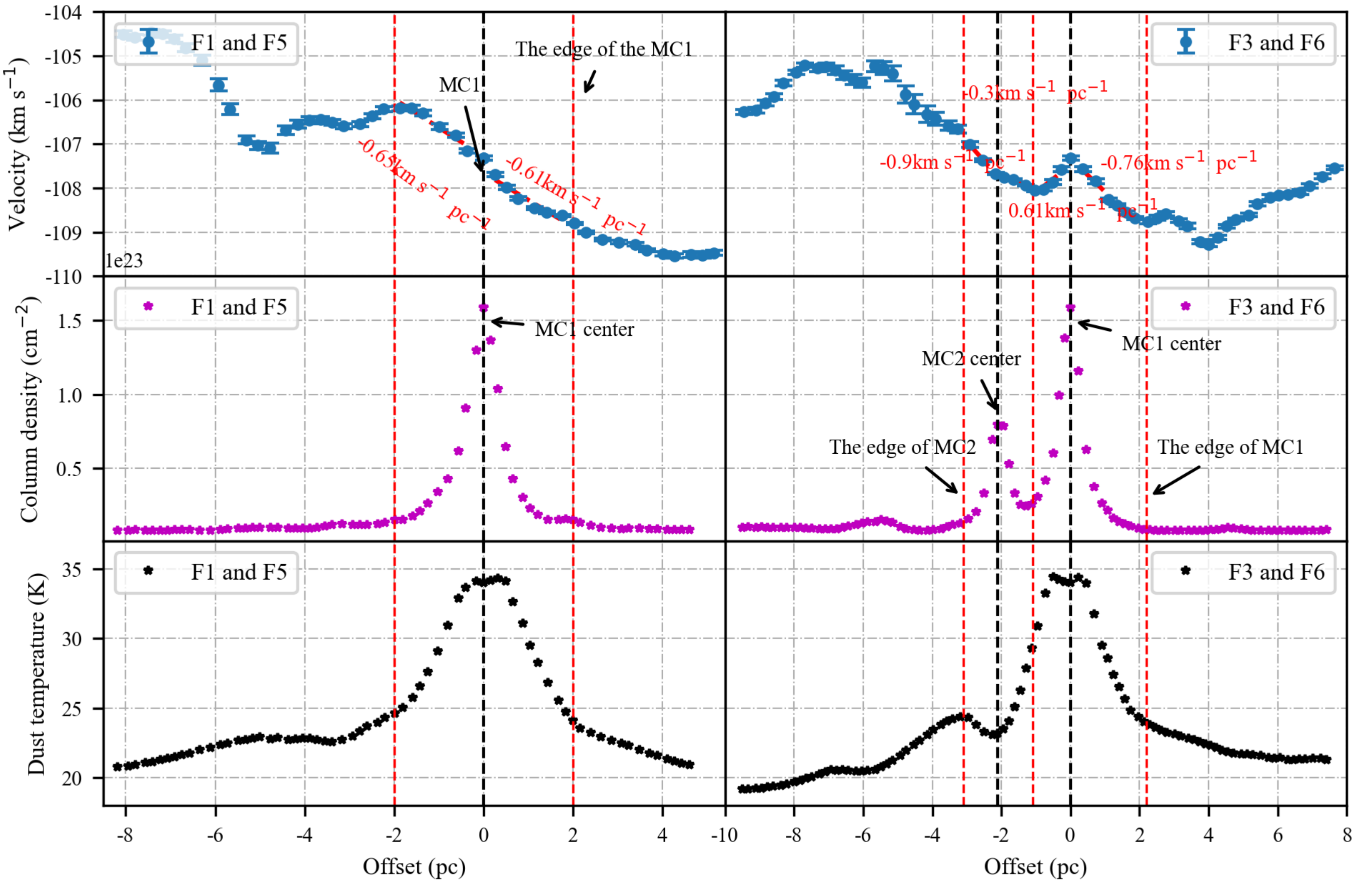

Fig. 6. P–V, position–column density, and position–dust temperature diagrams for F 1 + F 5 (left; for the filaments passing through clump MC 1, see Fig. 3; negative offset: extent of F 1, positive offset: range of F 5) and F 3 + F 6 (right; filaments passing through clumps MC 1 and MC 2; negative offset: extent of F 3, positive offset: range of F 6) within the filaments in G329. The dashed black lines mark the central positions of the clumps MC 1 and MC 2, while the dashed red lines indicate the boundary positions of MC 1 and MC 2.

because projection effects, inclination, and the adopted measurement paths affect the measured velocity structures.

4.3. From parsec-scale filaments to the hub: denser and more evolved physical conditions

Beyond their kinematic correspondence, the parsec-scale filaments and the IHFs also show clear differences in their physical properties. As summarized in Tables 1 and 3, the parsec-scale filaments have lengths of 4.6 - 8.2 pc and are, on average, substantially more massive (mean ∼2344 $M_{\odot}$) than the IHFs (mean ∼312 $M_{\odot}$). However, the IHFs, which trace denser gas on sub-parsec scales, exhibit systematically higher line masses and markedly steeper longitudinal velocity gradients (mean ∼3.27 km s^{-1} pc^{-1}) than the parsec-scale filaments (mean ∼0.26 km s^{-1} pc^{-1}). Although both scales yield mass accretion rates of the same order of magnitude according to Eq. (6), the much steeper gradients within the IHFs suggest that the dense gas in MC 1 is dynamically more complex than the surrounding parsec-scale gas. In this sense, the IHFs do not simply represent smaller versions of the parsec-scale filaments but instead trace a denser and physically distinct internal network within MC 1.

These differences may indicate that the gas enters a physically distinct environment upon reaching the hub, where local gravity likely becomes increasingly important. As discussed in Sect. 4.2, both the hydrogen column density and the longitudinal velocity gradient increase systematically toward the hub region, suggesting a progressive inward concentration of material. The hub, therefore, appears physically distinct from the surrounding parsec-scale filaments, while remaining kinematically linked to organized motions in the surrounding gas. In particular, F 1 and F 5 are directed toward MC 1, whereas F 3 and F 6 extend across the region containing both MC 1 and MC 2. The velocity gradients measured around MC 1 (∼0.66 km s^{-1} pc^{-1} on average) are slightly higher than those around MC 2 (∼0.60 km s^{-1} pc^{-1}; see Fig. 6), suggesting that the gas motions in MC 1 may be more concentrated. Combined with its higher dust temperature and an ultracompact H II region, this supports the view that MC 1 is in a more advanced and active star-forming stage than MC 2, while MC 2 remains at an earlier evolutionary stage. Taken together, these results suggest that filamentary gas motion likely plays an important role in building up the mass reservoir of MC 1 and in supporting ongoing massive star and cluster formation.

Such an interpretation is broadly consistent with the structural evolution discussed for systems such as Mon R2, where the hub has been interpreted as a network of short, dense filaments that may result from filament coalescence and reorganization (Kumar et al. 2022). More generally, recent work suggests that dense cluster-forming structures can become dynamically distinct from their parent molecular cloud environment as collapse proceeds (Peretto et al. 2023). The situation in G329 may reflect a similar transition: the surrounding parsec-scale filaments show projected velocity organization broadly consistent with motions toward the hub, while the gas dynamics within MC 1 appear to be increasingly influenced by the local gravitational potential.

Additional support for this picture comes from the velocity dispersion analysis. In Sect. 3.2, we discussed deriving the virial masses of the clumps under the conventional assumption that the observed velocity dispersion is entirely due to turbulent motions, providing support against gravitational collapse. However, recent studies have shown that in actively accreting structures, a significant fraction of the kinetic energy can instead arise from infall and accretion motions rather than from random turbulence (Morii et al. 2025; Vázquez-Semadeni et al. 2026). In this context, the observed velocity dispersion in MC 1 and MC 2 may not primarily reflect pressure support, and virial parameters derived under the turbulence-only assumption may not reliably indicate stability. Following Ballesteros-Paredes et al. (2011), the equipartition velocity dispersion expected for gravitationally collapsing gas, where kinetic and gravitational energies are comparable ($E_k \sim E_g$), is given by

$$\sigma_{eq}^2 = 2G\Sigma R_{eq}, \tag{16}$$

where Σ is the surface density and R_{eq} is the equivalent radius. Considering the uncertainties in clump masses, the kinetic and gravitational energies are close to equipartition ($\alpha_{vir} \approx 2$; see Table 2). Applying this relation to MC 1 and MC 2 yields $\sigma_{eq} \sim 3.07\,(\pm 0.69)$ and $\sim 2.11\,(\pm 0.47)\,\mathrm{km\,s^{-1}}$, respectively, comparable to the observed velocity dispersions ($\sigma_\mu = 2.26$ and $1.67\,\mathrm{km\,s^{-1}}$). This agreement suggests that the observed nonthermal motions may be broadly consistent with gravity-influenced dynamics, rather than with purely random turbulent support alone. Therefore, the dense hub environment should not be viewed simply as a passive endpoint of parsec-scale convergence, but as an actively evolving dynamical regime in which organized motions, collapse, and local reorganization all contribute.

4.4. Star formation and feedback in the more evolved hub node MC 1

MC 1 hosts an ultracompact H II region at its center (Fig. 4), indicating ongoing massive star formation. At the same time, the ALMA data suggest that organized gas motions remain active within MC 1, implying that feedback and local dense gas transport may coexist in this source.

Observations of CS (J=2-1) trace the dense gas distribution within MC 1. The integrated CS emission exhibits an elliptical shell morphology complementary to the $H_{40\alpha}$ emission (Fig. 7), indicating that it traces the compressed molecular shell produced by the expansion of the ultracompact H II region and stellar winds. Emissions of SiO (J=2-1) and SO (J=3(2)-2(1)) delineate the shell structure, suggesting that they originate from low-velocity shocks induced by the expansion of the H II region. Higher-resolution Band 6 SiO (J=5-4) and ^{12}CO (J=2-1) data further reveal two localized outflow structures in the northeastern part of the shell (Fig. F.1; Appendix F). The outflow lobes are spatially confined relative to the larger CS/SO/SiO shell and are associated with compact 1.3 mm continuum sources. These results imply that, although protostellar outflows can also excite SiO and SO emission, their contribution is confined to small localized areas, whereas the shell-like emission over most of the region is primarily driven by the expanding H II region.

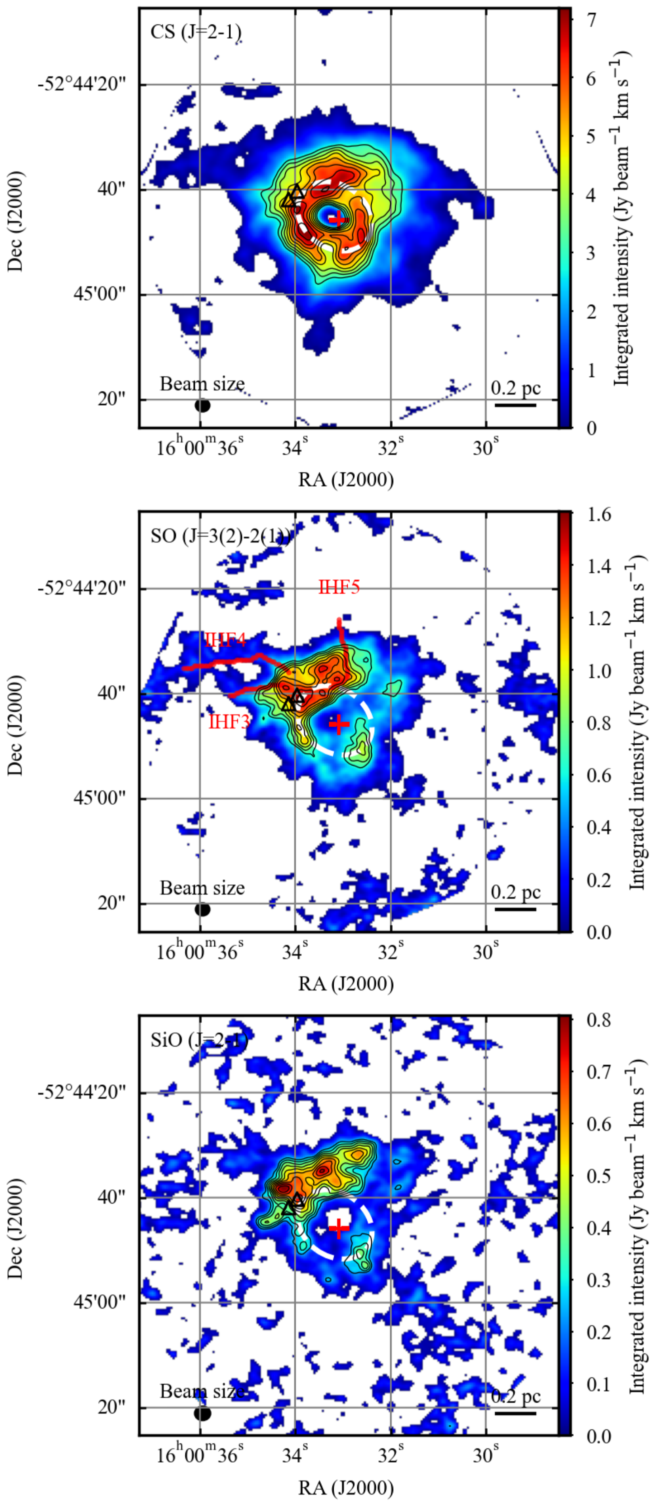

Fig. 7. *Top panel*: Integrated intensity map of CS (J=2-1). The black contours show the CS (J=2-1) integrated intensity, ranging from 40% to 96% of the peak value in 8% steps. *Middle panel*: Integrated intensity map of SO (J=3(2)-2(1)). The black contours show the SO (J=3(2)-2(1)) integrated intensity, ranging from 40% to 96% of the peak value in 8% steps. The red lines mark the spines of IHF 3, IHF 4, and IHF 5. *Bottom panel*: Integrated intensity map of SiO (J=2-1). The black contours show the SiO (J=2-1) integrated intensity, ranging from 30% to 94% of the peak value in 8% steps. In all three panels, the black triangles indicate the positions of the outflow-driving sources presented in Appendix F; the dashed white ellipse outlines the shell-like structure; and the red plus marks the peak position of the $H_{40\alpha}$ emission.

In addition to the feedback-driven shell, MC 1 contains a converging filamentary junction formed by IHF 3, IHF 4, and IHF 5. This junction is clearly visible in SiO, SO, and $H^{13}CO^+$ emission (Figs. 7 and 3) and likely marks a site of ongoing gas convergence and accumulation, where massive star formation is taking place. Notably, this converging filamentary structure shows little $H_{40\alpha}$ emission, suggesting that it is less affected by ionized feedback and may represent an earlier stage of star formation than the central ultracompact H II region.

Taken together, these observations suggest that massive star feedback in MC 1 primarily reshapes the dense gas locally, especially within the shell, but does not appear to erase the organized gas motions along the surrounding filamentary network. G329 therefore appears to represent an evolutionary stage in which dense gas organization can persist after the onset of massive star feedback, while feedback mainly modifies the local dense structure rather than dominating the global hub kinematics.

Although the ALMA analysis presented here focuses on MC 1, MC 2 is also part of the same hub and should be interpreted as a second, less evolved node rather than as a separate structure. The combined SEDIGISM and ALMA observations therefore support a conservative picture in which parsec-scale filaments converge toward a two-node hub, while the higher-resolution data reveal how the more evolved node, MC 1, is organized internally into dense IHFs and is reshaped by massive star feedback.

5. Conclusion

Using the ^{13}CO (J=2-1) data from the SEDIGISM survey for the molecular cloud G329, together with ALMA Band 3 and Band 6 observations of MC 1 – the more evolved clump within the hub – from the ATOMS and QUARKS surveys, we conducted a detailed investigation of the gas structures and kinematic properties within the HFS. Our main conclusions are as follows:

1. Molecular cloud G329 is a HFS composed of eight filaments and two dense clumps. The filaments have lengths ranging from ~4.6 (±0.7) to ~8.2 (±1.2) pc, with masses ranging from ~612 (±183) to ~3092 (±924) $M_\odot$. The two dense clumps, MC 1 and MC 2, have masses of ~4210 (±1259) and ~1483 (±443) $M_\odot$, respectively, with radii of ~1.23 (±0.18) pc and ~0.89 (±0.13) pc. Intense massive star formation activity is already present in MC 1.
2. ALMA observations reveal that the dense gas within MC 1 is organized into a network of sub-parsec IHFs. Based on $H^{13}CO^+$ (J=1-0) emission, seven IHFs were identified, with lengths ranging from ~0.29 (±0.04) to ~0.61 (±0.09) pc and masses ranging from ~156 (±47) to ~454 (±136) $M_\odot$. These results show that the more evolved hub node, MC 1, is internally resolved into a dense filamentary network.
3. Although the IHFs within MC 1 cannot be morphologically matched one-to-one with the filaments identified at lower angular resolution, their similar global velocity organization and systematic velocity gradients support a kinematic correspondence between the parsec-scale filaments and the sub-parsec IHFs. Compared with the parsec-scale filaments, the IHFs are more compact and exhibit steeper projected longitudinal velocity gradients, with a mean value of ~3.3 km s^{-1} pc^{-1}. The corresponding mass accretion rates are estimated to be on the same order of magnitude on the two scales. Together with the similar velocity organization, these results are consistent with possible parsec-scale filamentary gas transport toward the hub, with MC 1 tracing a denser and more evolved inner hub environment.
4. Observations of 3 mm continuum and $H_{40\alpha}$ emission reveal that stellar feedback in MC 1 has created an ultracompact H II region and a surrounding molecular shell. Molecular outflows traced by SiO (J=5-4) and ^{12}CO (J=2-1) were also detected on the shell. These findings indicate that shells swept up by the H II region may enhance star formation activity in the surrounding dense gas.
5. The combined SEDIGISM and ALMA observations are consistent with a conservative filamentary gas transport picture in G329. The parsec-scale filaments converge toward a central hub region containing two evolutionary-offset nodes, MC 1 and MC 2. In the more evolved node, MC 1, the dense gas is organized into a compact internal filamentary network and shows a velocity organization broadly related to that of the surrounding parsec-scale filaments. Together with an ultracompact H II region, shell-like molecular emission, and outflows, these results suggest that possible filamentary gas transport and massive star feedback coexist during the evolution of MC 1.

Finally, we note the limitations of this study. Molecular cloud rotation is commonly observed (Fleck 1989; Phillips 1999; Li et al. 2017; Braine et al. 2018, 2020; Rani et al. 2024), and both longitudinal motions and rotation may coexist in the G329 molecular cloud. Therefore, the projected inflow velocity inferred from the velocity gradients might be affected by rotational motion. Moreover, the angular resolution of current large-scale surveys such as SEDIGISM remains insufficient to resolve the fine filamentary structures within molecular clouds, which to some extent limits direct comparisons with the higher-resolution IHFs revealed by ALMA observations. Future wide-field, high-resolution observations will be essential to disentangle the relative roles of rotation and longitudinal gas motions and to better relate the gas kinematics of molecular clouds to their central star-forming regions.

Acknowledgements. This work was mainly supported by the National Key R&D Program of China under grant Nos. 2022YFA1603103 and 2023YFA1608002, the National Natural Science Foundation of China (NSFC) under grant No. 12373029, and the Central Guidance for Local Science and Technology Development Fund under grant No. ZYYD2025ZY23. This work was also partially supported by the Tianshan Talent Training Program under grant No. 2024TSYCTD0013, the NSFC under grant Nos. 12173075, 12103082, and 12403033, XBZG-ZDSYS-202212, the Natural Science Foundation of Xinjiang Uygur Autonomous Region under grant No. 2023D01A11, and the Science Committee of the Ministry of Science and Higher Education of the Republic of Kazakhstan (Grant No. AP26102915). G.W. acknowledges support from the Xinjiang Tianchi Talents Program, the Xinjiang Key Laboratory of Radio Astrophysics under grant No. 2023D04033, the National SKA Program of China under grant No. 2025SKA0140100, the Youth Innovation Promotion Association CAS, the CAS-ANSO Fellowship under grant No. CAS-ANSO-FA-2024-06, and the Tianchi Talent Project of Xinjiang Uygur Autonomous Region. DL is a New Cornerstone Investigator and is supported by the NSFC under grant No.11988101. H.-L. Liu is supported by Yunnan Fundamental Research Project (grant No. 202301AT070118, 202401AS070121), and by Xingdian Talent Support Plan–Youth Project. SRD acknowledges support from the Fondecyt Postdoctoral fellowship (project code 3220162) and ANID BASAL project FB210003. WAB has been supported by the Chinese Academy of Sciences President International Fellowship Initiative by Grant No. 2023VMA0030. AH thanks the support of the S. N. Bose National Centre for Basic Sciences under the Department of Science and Technology, Govt. of India, and the CSIR-HRDG, Govt. of India for funding the fellowship. GG gratefully acknowledges support by the ANID BASAL project FB210003. This paper makes use of the following ALMA data: ADS/JAO.ALMA 2019.1.00685.S. ALMA is a partnership of ESO (representing its member states), NSF (USA), and NINS (Japan), together with NRC (Canada), MOST and ASIAA (Taiwan), and KASI (Republic of Korea), in cooperation with the Republic of Chile. The Joint ALMA Observatory is operated by ESO, AUI/NRAO, and NAOJ. This publication is also based on data acquired with the APEX under programs 092.F-9315 and 193.C-0584. APEX collaborates with the Max-Planck-Institut fur Radioastronomie, the European Southern Observatory, and the Onsala Space Observatory. The processed data products are available from the SEDIGISM survey database, which was constructed by James Urquhart and hosted by the Max Planck Institute for Radio Astronomy. We also thank the referee for the careful reading of the manuscript and for the many valuable comments and suggestions, which have significantly improved the clarity and quality of this paper.

Data availability

The ALMA archival data in this paper can be downloaded from ADS/JAO.ALMA 2019.1.00685.S at ALMA science archive. The *Spitzer* GLIMPSE legacy survey data can be downloaded at NASA/IPAC Infrared Science Archive. The *Herschel* key project Hi-GAL survey data can be downloaded at Herschel Science Archive. The CO archival data in this work can be downloaded at Structure, Excitation and Dynamics of the Inner Galactic Interstellar Medium.

References

André, P., Di Francesco, J., Ward-Thompson, D., et al. 2014, in Protostars and Planets VI, ed. H. Beuther, R. S. Klessen, C. P. Dullemond, & T. Henning, 27–51
André, P., Men'shchikov, A., Bontemps, S., et al. 2010, A&A, 518, L102
Aniano, G., Draine, B. T., Gordon, K. D., & Sandstrom, K. 2011, PASP, 123, 1218
Ballesteros-Paredes, J., Hartmann, L. W., Vázquez-Semadeni, E., Heitsch, F., & Zamora-Avilés, M. A. 2011, MNRAS, 411, 65
Benjamin, R. A., Churchwell, E., Babler, B. L., et al. 2003, PASP, 115, 953
Bernard, J. P., Paradis, D., Marshall, D. J., et al. 2010, A&A, 518, L88
Bhadari, N. K., Dewangan, L. K., Pirogov, L. E., & Ojha, D. K. 2020, ApJ, 899, 167
Braine, J., Hughes, A., Rosolowsky, E., et al. 2020, A&A, 633, A17
Braine, J., Rosolowsky, E., Gratier, P., Corbelli, E., & Schuster, K. F. 2018, A&A, 612, A51
Carey, S. J., Noriega-Crespo, A., Mizuno, D. R., et al. 2009, PASP, 121, 76
Chandrasekhar, S. 1951, Proceedings of the Royal Society of London Series A, 210, 26
Chen, H.-R. V., Zhang, Q., Wright, M. C. H., et al. 2019, ApJ, 875, 24
Colombo, D., Rosolowsky, E., Duarte-Cabral, A., et al. 2019, MNRAS, 483, 4291
Fazio, G. G., Hora, J. L., Allen, L. E., et al. 2004, ApJS, 154, 10
Fiege, J. D. & Pudritz, R. E. 2000, MNRAS, 311, 85
Fleck, Jr., R. C. 1989, AJ, 97, 783
Garden, R. P., Hayashi, M., Gatley, I., Hasegawa, T., & Kaifu, N. 1991, ApJ, 374, 540
Griffin, M. J., Abergel, A., Abreu, A., et al. 2010, A&A, 518, L3
Güsten, R., Nyman, L. Å., Schilke, P., et al. 2006, A&A, 454, L13
Hacar, A., Alves, J., Tafalla, M., & Goicoechea, J. R. 2017, A&A, 602, L2
Hacar, A., Clark, S. E., Heitsch, F., et al. 2023, in Astronomical Society of the Pacific Conference Series, Vol. 534, Protostars and Planets VII, ed. S. Inutsuka, Y. Aikawa, T. Muto, K. Tomida, & M. Tamura, 153
Hacar, A., Konietzka, R., Seifried, D., et al. 2025, A&A, 694, A69
He, Y.-X., Zhou, J.-J., Esimbek, J., et al. 2015, MNRAS, 450, 1926
Hildebrand, R. H. 1983, QJRAS, 24, 267
Hoq, S., Jackson, J. M., Foster, J. B., et al. 2013, ApJ, 777, 157
Inutsuka, S.-i. & Miyama, S. M. 1997, ApJ, 480, 681
Karim, R. L., Pound, M. W., Tielens, A. G. G. M., et al. 2023, AJ, 166, 240
Kauffmann, J., Bertoldi, F., Bourke, T. L., Evans, N. J., I., & Lee, C. W. 2008, A&A, 487, 993
Kauffmann, J. & Pillai, T. 2010, ApJ, 723, L7
Kirk, H., Myers, P. C., Bourke, T. L., et al. 2013, ApJ, 766, 115
Koch, E. W. & Rosolowsky, E. W. 2015, MNRAS, 452, 3435
Kumar, M. S. N., Arzoumanian, D., Inutsuka, S., Furuya, R., & Bhadari, N. K. 2025, A&A, 703, A74
Kumar, M. S. N., Arzoumanian, D., Men'shchikov, A., et al. 2022, A&A, 658, A114
Kumar, M. S. N., Palmeirim, P., Arzoumanian, D., & Inutsuka, S. I. 2020, A&A, 642, A87
Li, D. L., Esimbek, J., Zhou, J. J., et al. 2014, A&A, 567, A10
Li, G.-X., Urquhart, J. S., Leurini, S., et al. 2016, A&A, 591, A5
Li, G.-X., Wyrowski, F., & Menten, K. 2017, A&A, 598, A96
Li, S., Sanhueza, P., Lee, C. W., et al. 2022, ApJ, 926, 165
Lin, Y., Liu, H. B., Li, D., et al. 2016, ApJ, 828, 32
Liu, H. B., Quintana-Lacaci, G., Wang, K., et al. 2012, ApJ, 745, 61
Liu, H.-L., Sanhueza, P., Liu, T., et al. 2020a, ApJ, 901, 31
Liu, H.-L., Tej, A., Liu, T., et al. 2022a, MNRAS, 510, 5009
Liu, H.-L., Tej, A., Liu, T., et al. 2023, MNRAS, 522, 3719
Liu, R., Liu, T., Chen, G., et al. 2022b, MNRAS, 511, 3618
Liu, R., Liu, T., Jiménez-Serra, I., et al. 2025, MNRAS, 536, 1894
Liu, T., Evans, N. J., Kim, K.-T., et al. 2020b, MNRAS, 496, 2821
Liu, T., Evans, N. J., Kim, K.-T., et al. 2020c, MNRAS, 496, 2790
Liu, X., Liu, T., Zhu, L., et al. 2024, Research in Astronomy and Astrophysics, 24, 025009
Ma, Y., Zhou, J., Esimbek, J., et al. 2023, A&A, 676, A15
MacLaren, I., Richardson, K. M., & Wolfendale, A. W. 1988, ApJ, 333, 821
Maity, A. K., Dewangan, L. K., Bhadari, N. K., et al. 2025, AJ, 169, 56
Mather, J. C., Cheng, E. S., Cottingham, D. A., et al. 1994, ApJ, 420, 439
Mattern, M., Kainulainen, J., Zhang, M., & Beuther, H. 2018a, A&A, 616, A78
Mattern, M., Kauffmann, J., Csengeri, T., et al. 2018b, A&A, 619, A166
Molinari, S., Swinyard, B., Bally, J., et al. 2010a, A&A, 518, L100
Molinari, S., Swinyard, B., Bally, J., et al. 2010b, PASP, 122, 314
Morii, K., Sanhueza, P., Csengeri, T., et al. 2025, ApJ, 979, 233
Myers, P. C. 2009, ApJ, 700, 1609
Ostriker, J. 1964, ApJ, 140, 1056
Palmeirim, P., André, P., Kirk, J., et al. 2013, A&A, 550, A38
Pan, S., Liu, H.-L., & Qin, S.-L. 2024, ApJ, 960, 76
Peretto, N., Fuller, G. A., Duarte-Cabral, A., et al. 2013, A&A, 555, A112
Peretto, N., Rigby, A. J., Louvet, F., et al. 2023, MNRAS, 525, 2935
Phillips, J. P. 1999, A&AS, 134, 241
Pilbratt, G. L., Riedinger, J. R., Passvogel, T., et al. 2010, A&A, 518, L1
Poglitsch, A., Waelkens, C., Bauer, O. H., et al. 2010, in 38th COSPAR Scientific Assembly, Vol. 38, 13
Rani, R., Li, J.-L., Moore, T. J. T., et al. 2024, MNRAS, 532, 2501
Reid, M. J., Dame, T. M., Menten, K. M., & Brunthaler, A. 2016, ApJ, 823, 77
Reid, M. J., Menten, K. M., Brunthaler, A., et al. 2019, ApJ, 885, 131
Rieke, G. H., Young, E. T., Engelbracht, C. W., et al. 2004, ApJS, 154, 25
Rigby, A. J., Moore, T. J. T., Eden, D. J., et al. 2019, A&A, 632, A58
Sadavoy, S. I., Keto, E., Bourke, T. L., et al. 2018, ApJ, 852, 102
Schneider, N., Csengeri, T., Hennemann, M., et al. 2012, A&A, 540, L11
Schuller, F., Csengeri, T., Urquhart, J. S., et al. 2017, A&A, 601, A124
Shimajiri, Y., André, P., Braine, J., et al. 2017, A&A, 604, A74
Tiwari, M., Karim, R., Pound, M. W., et al. 2021, ApJ, 914, 117
Treviño-Morales, S. P., Fuente, A., Sánchez-Monge, Á., et al. 2019, A&A, 629, A81
Urquhart, J. S., Csengeri, T., Wyrowski, F., et al. 2014, A&A, 568, A41
Urquhart, J. S., König, C., Giannetti, A., et al. 2018, MNRAS, 473, 1059
Vázquez-Semadeni, E., Palau, A., Gómez, G. C., et al. 2026, MNRAS, 547, staf2059
Wang, K., Testi, L., Ginsburg, A., et al. 2015, MNRAS, 450, 4043
Wang, K., Zhang, Q., Testi, L., et al. 2014, MNRAS, 439, 3275
Wang, K., Zhang, Q., Wu, Y., & Zhang, H. 2011, ApJ, 735, 64
Wu, G., Qiu, K., Esimbek, J., et al. 2018, A&A, 616, A111
Xu, F., Wang, K., Liu, T., et al. 2024, Research in Astronomy and Astrophysics, 24, 065011
Xu, F.-W., Wang, K., Liu, T., et al. 2023, MNRAS, 520, 3259
Yang, A. Y., Urquhart, J. S., Wyrowski, F., et al. 2022, A&A, 658, A160
Yang, D., Liu, H.-L., Tej, A., et al. 2023, ApJ, 953, 40
Yuan, J., Li, J.-Z., Wu, Y., et al. 2018, ApJ, 852, 12
Zhang, C., Zhu, F.-Y., Liu, T., et al. 2023, MNRAS, 520, 3245
Zhang, S., Liu, T., Wang, K., et al. 2024a, MNRAS, 535, 1364
Zhang, W., Zhou, J., Esimbek, J., et al. 2024b, A&A, 688, A99
Zhou, J.-W., Liu, T., Evans, N. J., et al. 2022, MNRAS, 514, 6038
Zucker, C. & Chen, H. H.-H. 2018, ApJ, 864, 152

[1] State Key Laboratory of Radio Astronomy and Technology, Xinjiang Astronomical Observatory, CAS, 150 Science 1-Street, Urumqi, Xinjiang 830011, PR China
[2] University of Chinese Academy of Sciences, Beijing 100049, PR China
[3] Xinjiang Key Laboratory of Radio Astrophysics, Urumqi 830011, PR China
[4] Shanghai Astronomical Observatory, Chinese Academy of Sciences, 80 Nandan Road, Shanghai 200030, PR China
[5] School of Physics and Astronomy, Yunnan University, Kunming 650091, PR China
[6] Instituto de Radioastronomía y Astrofísica, Universidad Nacional Autónoma de México, Antigua Carretera a Pátzcuaro 8701, Ex-Hda. San José de la Huerta, 58089 Morelia, Michoacán, México
[7] Max-Planck-Institut für Radioastronomie, Auf dem Hügel 69, 53121 Bonn, Germany
[8] Departamento de Astronomia, Universidad de Chile, Las Condes, 7591245 Santiago, Chile
[9] National Astronomical Observatories, Chinese Academy of Sciences, A20 Datun Road, Chaoyang District, Beijing 100101, PR China
[10] Department of Astronomy, Tsinghua University, Beijing 100084, PR China
[11] Chinese Academy of Sciences South America Center for Astronomy, National Astronomical Observatories, CAS, Beijing 100101, PR China
[12] Kavli Institute for Astronomy and Astrophysics, Peking University, 5 Yiheyuan Road, Haidian District, Beijing 100871, PR China
[13] Department of Astronomy, Peking University, 100871 Beijing, PR China
[14] Physical Research Laboratory, Navrangpura, Ahmedabad 380009, India
[15] Rosseland Centre for Solar Physics, University of Oslo, PO Box 1029 Blindern, 0315 Oslo, Norway
[16] Institute of Theoretical Astrophysics, University of Oslo, PO Box 1029 Blindern, 0315 Oslo, Norway
[17] Korea Astronomy and Space Science Institute, 776 Daedeokdae-ro, Yuseong-gu, Daejeon 34055, Republic of Korea
[18] Department of Mathematical Sciences, University of South Africa, Cnr Christian de Wet Rd and Pioneer Avenue, Florida Park, 1709, Roodepoort, South Africa
[19] Department of Physics and Astronomy, Faculty of Physical Sciences, University of Nigeria, Carver Building, 1 University Road, Nsukka 410001, Nigeria
[20] Instituto de Astronomía, Universidad Católica del Norte, Av. Angamos 0610, Antofagasta, Chile
[21] University of Science and Technology, Korea (UST), 217 Gajeong-ro, Yuseong-gu, Daejeon 34113, Republic of Korea
[22] S. N. Bose National Centre for Basic Sciences, Block-JD, Sector-III, Salt Lake City, Kolkata 700106, India
[23] Institute of Physics and Astronomy, Eötvös Loränd University, Pázmány Péter sétány 1/A, H-1117 Budapest, Hungary
[24] Energetic Cosmos Laboratory, Nazarbayev University, 53 Kabanbay batyr Ave., Astana 010000, Kazakhstan
[25] Institute of Experimental and Theoretical Physics, Al-Farabi Kazakh National University, Almaty 050040, Kazakhstan

Appendix A: Identification and velocity-based refinement of filaments in G329

This section presents the identification and velocity-based refinement of filaments in the G329 molecular cloud. Figure A.1 compares the initial column-density skeletons with the final adopted filament spines. The left panel shows the skeletons identified with *FilFinder* on the hydrogen column density map, while the right panel shows the final adopted spines overlaid on the ^{13}CO (J=2-1) integrated intensity distribution. The column-density skeletons provide the initial morphological reference for the subsequent analysis, and the ^{13}CO (J=2-1) integrated intensity and channel map information is used to check and refine the final spines for spatial and velocity coherence.

Figure A.2 presents the ^{13}CO (J=2-1) channel maps of the G329 molecular cloud, with a velocity interval of 0.5 km s^{-1} between adjacent channels. Based on the velocity coherence along the filaments, the initial column-density skeletons identified by *FilFinder* were subsequently refined using the channel maps. Specifically, we examined the velocity continuity along each candidate filament and applied minor manual adjustments to the skeletons when necessary, ensuring that the final adopted spines follow coherent velocity structures rather than relying solely on automated morphological extraction. Only structures exhibiting continuous velocity patterns were retained as filaments (see Fig. A.2 and Table A.1). Therefore, the filament spines adopted throughout the main text correspond to velocity-consistent skeletons constrained by the ^{13}CO (J=2-1) integrated intensity distribution and channel maps, with the column density map serving as the initial morphological reference. The channel maps further reveal the velocity distribution of molecular gas along each filament (see Table A.1), demonstrating both velocity coherence and the presence of velocity gradients across the filaments.

Table A.1. Velocity identification of filaments in the CO channel maps.

-	F 1	F 2	F 3	F 4	F 5	F 6	F 7	F 8
Dominant velocity range$^{(a)}$ (km s^{-1})	-106.0 to -103.5	-108.0 to -105.5	-105.5 to -103.5	-108.5 to -105.0	-111.0 to -109.5	-109.5 to -107.5	-109.5 to -107.5	-108.5 to -106.5
Representative channel$^{(b)}$ (km s^{-1})	-104.5	-106.5	-104.5	-106.5	-110.0	-108.5	-108.5	-107.0

Notes. $^{(a)}$ Velocity interval over which each filament is most clearly detected in the ^{13}CO (J=2-1) channel maps shown in Fig. A.2. This range is determined empirically from the prominence and continuity of the filamentary emission and is intended as a descriptive guide.
$^{(b)}$ Velocity channel at which the corresponding filament appears most prominently in the channel maps and is therefore used as a representative example for visual identification.

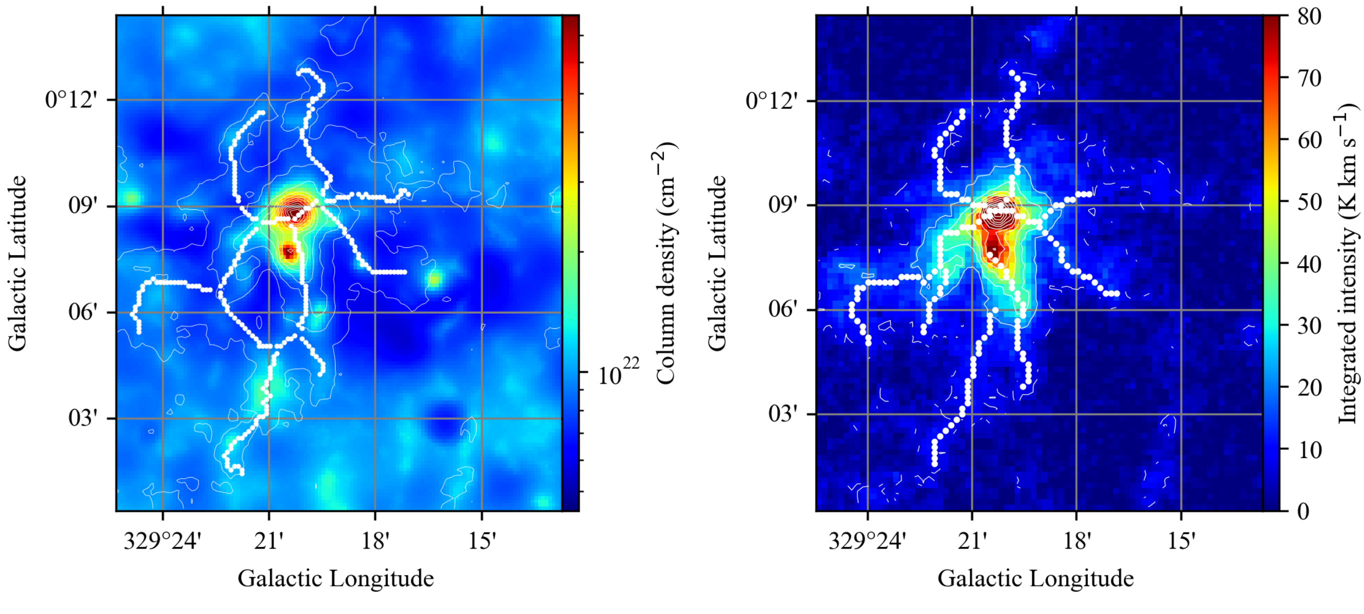

Fig. A.1. Left: Initial filament skeletons (white dots) identified using *FilFinder* on the hydrogen column density map and overlaid on the column density distribution. Right: Final adopted filament spines (white dots) overlaid on the ^{13}CO (J=2-1) integrated intensity distribution. These spines were obtained after the initial skeletons were checked and refined using the ^{13}CO (J=2-1) integrated intensity distribution and velocity-coherence information from the channel maps. The contours indicate the integrated intensity values for ^{13}CO (J=2-1).

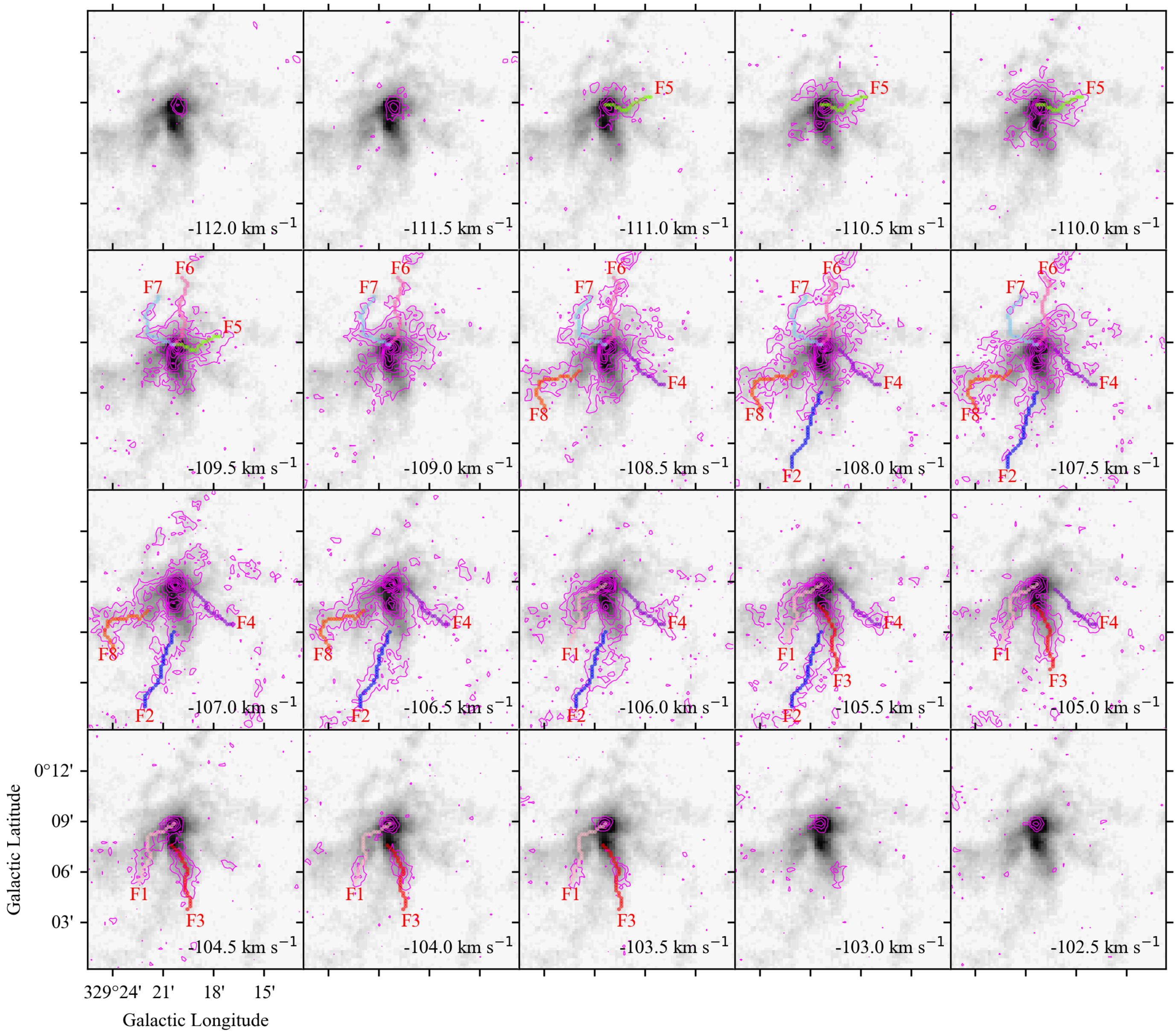

Fig. A.2. Channel maps of ^{13}CO (J=2-1). The grayscale map represents the distribution of integrated intensity for ^{13}CO (J=2-1), and the magenta contours depict the outlines of gas emission intensity at each velocity channel. The colored lines represent the filament spines.

Appendix B: Spectral analysis in the G329

This section presents the spectral lines at certain positions on the filaments and the average spectral lines of two clumps, MC 1 and MC 2. We used Gaussian fitting to obtain their centroid velocities and velocity dispersions:

$$f(x) = Ae^{-\frac{(x-\mu)^2}{2\sigma^2}}. \tag{B.1}$$

Figure B.1 shows the average spectra of ^{13}CO (J=2-1) and C^{18}O (J=2-1) for MC 1 and MC 2, in the molecular cloud. Spectral analysis indicates that they all exhibit single velocity components. From Gaussian fitting, the centroid velocities of ^{13}CO (J=2-1) and C^{18}O (J=2-1) in MC 1 are ∼-107.69 km s^{-1} and ∼-107.45 km s^{-1}, respectively, with velocity dispersions of ∼2.55 km s^{-1} and ∼2.26 km s^{-1}. In MC 2, the centroid velocities of ^{13}CO (J=2-1) and C^{18}O (J=2-1) are ∼-107.63 km s^{-1} and ∼-107.59 km s^{-1}, respectively, with velocity dispersions of ∼1.82 km s^{-1} and ∼1.67 km s^{-1}. The velocity distributions of MC 1 and MC 2 are generally consistent. Still, the velocity dispersion in MC 1 is significantly higher than in MC 2, likely due to the stronger star formation activity in MC 1.

Figure B.2 presents the ^{13}CO (J=2-1) spectra extracted at representative positions along the filament spines. For each filament, two positions are analyzed: an inner position closer to the hub (labeled as "a") and an outer position farther from the hub (labeled as "b"). In addition, spectra toward the two central hub clumps, MC 1 (labeled as H1) and MC 2 (labeled as H2), are shown for

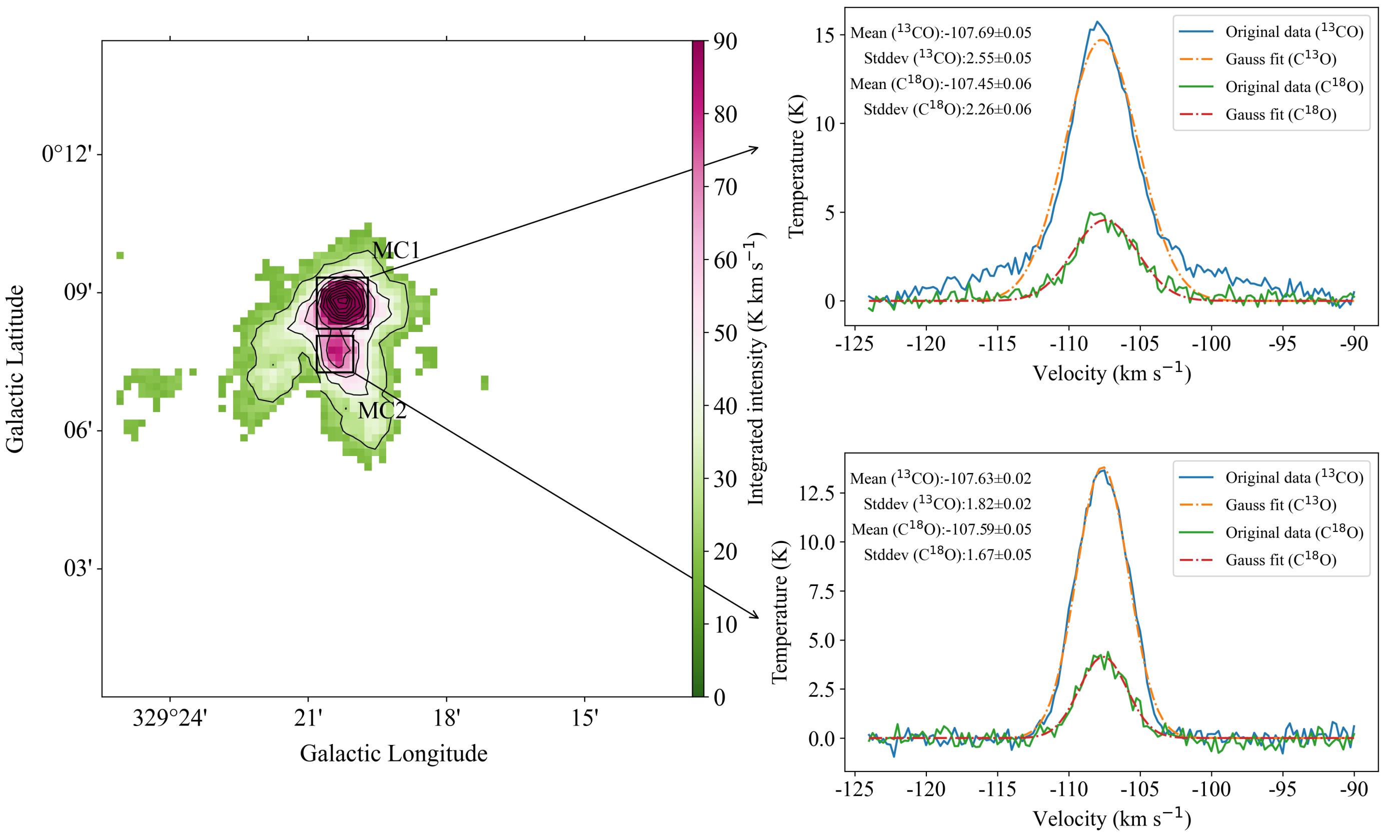

Fig. B.1. Average spectra for MC 1 and MC 2. Left: Color map of the ^{13}CO (J=2-1) integrated intensity at the center of the molecular cloud, with black contours representing 5% to 93% of the peak integrated intensity in 8% steps. The black rectangles indicate the regions of MC 1 and MC 2. Right: Averaged spectra of ^{13}CO (J=2-1) (blue) and C^{18}O (J=2-1) (green) for MC 1 (upper) and MC 2 (lower).

comparison. As shown in Fig. B.2, the line centroids differ between the inner and outer positions in several filaments, consistent with the projected velocity variations inferred along the filament spines. The line widths also tend to be smaller at the outer positions than at the inner positions, although this trend is not uniform for all filaments. The fitted line parameters at these representative positions are summarized in Table B.1.

Table B.1. Velocity information at different positions in the G329 molecular cloud.

-	H1	H2	F1a	F1b	F2a	F2b	F3a	F3b	F4a	F4b	F5a	F5b	F6a	F6b	F7a	F7b	F8a	F8b
V_{peak}[(a)]	-107.6	-107.7	-106.3	-106.4	-107.3	-106.5	-106.4	-105.0	-107.7	-105.4	-109.0	-109.6	-108.9	-108.8	-108.2	-108.6	-107.4	-107.3
Sigma[(b)]	3.2	1.8	1.5	1.2	1.2	1.1	2.4	0.9	1.4	0.9	1.4	0.9	1.6	0.8	1.2	0.9	1.3	1.3

Notes. H1 and H2 denote the central positions of MC 1 and MC 2, respectively. For each filament, position "a" marks the point closer to the hub, whereas position "b" marks the point farther from the hub.
[(a)] The center velocity obtained from the Gaussian fit in kilometers per second.
[(b)] The standard deviation obtained from the Gaussian fit in kilometers per second.

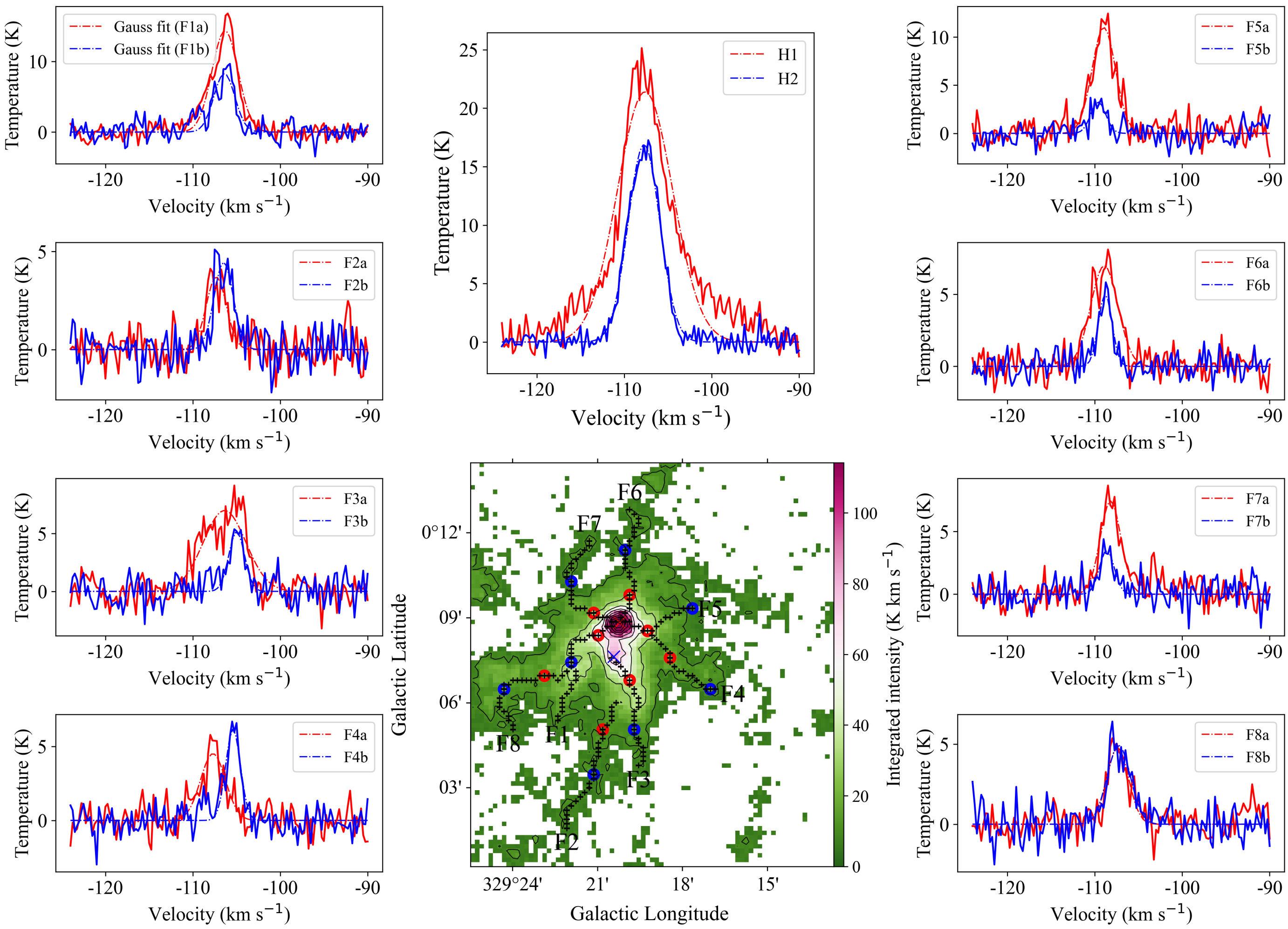

Fig. B.2. Color map representing the integrated intensity values for ^{13}CO (J=2-1). The contours range from 5% to 95% of the peak integrated intensity in 10% intervals. The black scatter points indicate the spines of the eight identified filaments. For each filament, two representative positions are marked: an inner position closer to the hub (labeled "a", shown in red) and an outer position farther from the hub (labeled "b", shown in blue). In addition, the central positions of MC 1 and MC 2 are marked by red and blue crosses and labeled as H1 and H2, respectively. Surrounding panels: ^{13}CO (J=2-1) spectra extracted at these representative positions. Gaussian fits to the spectra were used to derive the centroid velocities and velocity dispersions.

Appendix C: The position–velocity diagram on filaments

This section presents the distribution of velocity, velocity dispersion, column density, and dust temperature along the spines of filaments. Along the spines of the filaments, we performed Gaussian fits to the averaged molecular spectra within the filament width, with the central position being the point on the spine. This was done while moving outward from the center of the hub (MC 1 or MC 2). Consequently, we obtained the peak velocity and velocity dispersion for each position. Furthermore, following the spines of filaments from the hub center outward, we calculated the mean hydrogen molecule column density and dust temperature within the averaged filament width at each position. This allowed us to determine the hydrogen molecule column density and dust temperature for each position.

Figure C.1 illustrates the variations in velocity, velocity dispersion, dust temperature, and molecular hydrogen column density along the spine of F 1 from the center of MC 1 outward. Within $\sim$1.70 pc of the center, both the molecular hydrogen column density and dust temperature increase significantly; thus, we define the distance of $\sim$1.70 pc from the center as the edge of MC 1. Within MC 1, the velocity gradient and molecular hydrogen column density gradient are $\sim$0.78 km s^{-1} pc^{-1} and $\sim$-7.19 $\times 10^{22}$ cm^{-2} pc^{-1}, respectively. Outside MC 1, the velocity gradient and molecular hydrogen column density gradient are $\sim$0.36 km s^{-1} pc^{-1} and $\sim$-9.70 $\times 10^{20}$ cm^{-2} pc^{-1}, respectively. In the P–V diagram of F 3, the edge of MC 2 is approximately $\sim$1.70 pc away. The velocity gradients inside and outside MC 2 are similar, measuring $\sim$0.59 and $\sim$0.01 km s^{-1} pc^{-1}, respectively. Along the filament spine, the molecular hydrogen column density gradients inside and outside MC 2 are $\sim$-3.09 $\times 10^{22}$ cm^{-2} pc^{-1} and $\sim$-5.87 $\times 10^{19}$ cm^{-2} pc^{-1} (see Fig. C.2). F 4 is a sub-filament of F 5. Along the filament outward, the linear decrease in hydrogen column density has a gradient of $\sim$-7.95 $\times 10^{20}$ cm^{-2} pc^{-1}, while the velocity gradient linearly increases with a gradient of $\sim$0.82 km s^{-1} pc^{-1} (see Fig. C.3). The MC 1 edge of filament F 5 is located at $\sim$1.70 pc. The velocity gradients inside and outside MC 1 are $\sim$-0.81 and $\sim$-0.30 km s^{-1} pc^{-1}, respectively. The hydrogen column density gradients inside and outside MC 1 are $\sim$-7.43 and $\sim$-0.19 $\times 10^{22}$ cm^{-2} pc^{-1}, respectively (see Fig. C.4). The MC 1 edge of filament F 6 is located at $\sim$1.70 pc. The velocity gradients inside and outside MC 1 are $\sim$-0.87 and $\sim$0.19 km s^{-1} pc^{-1}, respectively. The hydrogen column density gradients inside and outside MC 1 are $\sim$-7.49 and $\sim$-0.01 $\times 10^{22}$ cm^{-2} pc^{-1}, respectively (see Fig. C.5). The MC 1 edge of filament F 7 is located at $\sim$2.20 pc. The velocity gradients inside and outside MC 1 are $\sim$-0.87 and $\sim$0.20 km s^{-1} pc^{-1}, respectively. The hydrogen column density gradients inside and outside MC 1 are $\sim$-5.79 and $\sim$0.04 $\times 10^{22}$ cm^{-2} pc^{-1}, respectively (see Fig. C.6).

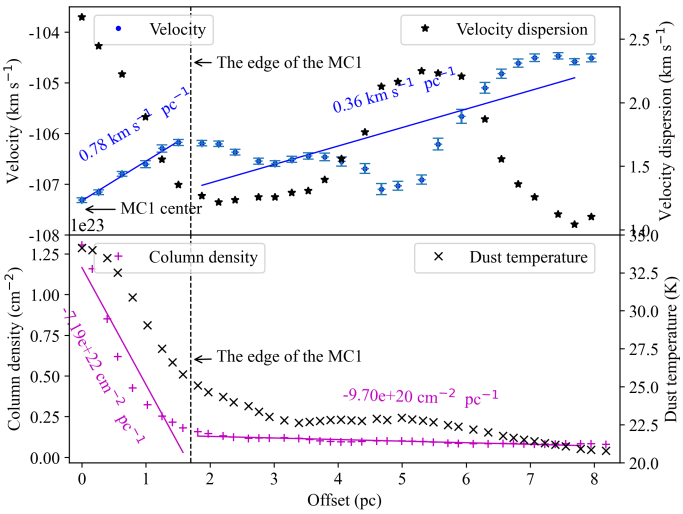

Fig. C.1. Variations in line-of-sight velocity, velocity dispersion, hydrogen molecule column density, and dust temperature along the F 1 spine, extending outward from MC 1.

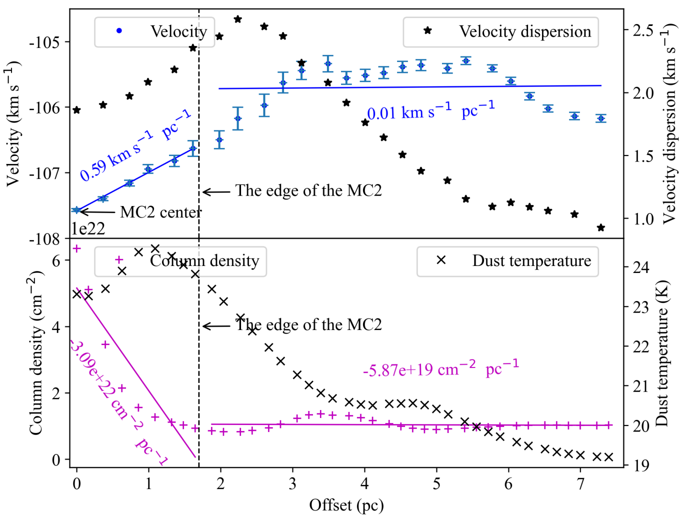

Fig. C.2. Variations in line-of-sight velocity, velocity dispersion, hydrogen molecule column density, and dust temperature along the F 3 spine, extending outward from MC 2.

Table C.1. Gradient parameters in filaments.

Source ID	$\nabla V_{\parallel}$[a] (km s^{-1} pc^{-1})	$\nabla V_{\rm in}$[b] (km s^{-1} pc^{-1})	$\nabla V_{\rm out}$[c] (km s^{-1} pc^{-1})	∇N[d] ($\times 10^{22}$ cm^{-2} pc^{-1})	$\nabla N_{\rm in}$[e] ($\times 10^{22}$ cm^{-2} pc^{-1})	$\nabla N_{\rm out}$[f] ($\times 10^{22}$ cm^{-2} pc^{-1})	∇T[g] (K pc^{-1})	$\nabla T_{\rm in}$[h] (K pc^{-1})	$\nabla T_{\rm out}$[i] (K pc^{-1})
F 1	0.29	0.78	0.36	-0.70	-7.19	-0.10	-1.25	-5.80	-0.52
F 2	0.10	-	-	0.03	-	-	-0.26	-	-
F 3	0.22	0.59	0.01	-0.26	-3.09	0.01	-0.76	0.54	-0.66
F 4	0.82	-	-	-0.08	-	-	0.22	-	-
F 5	-0.39	-0.81	-0.30	-1.78	-7.43	-0.19	-3.10	-5.67	-1.26
F 6	0.01	-0.87	0.19	-0.65	-7.49	-0.01	-1.43	-6.11	-0.57
F 7	-0.16	-0.87	0.20	-0.76	-5.79	0.04	-1.29	-5.71	-0.29
F 8	-0.09	-	-	0.02	-	-	-0.32	-	-

Notes. [a] Velocity gradient along the entire filament:$\Delta V/\Delta l$. [b] Velocity gradient along the filament spine within the hub. [c] Velocity gradient along the filament spine outside the hub. [d] Hydrogen column density gradient along the entire filament:$\Delta N/\Delta l$. [e] Hydrogen column density gradient along the filament spine within the hub. [f] Hydrogen column density gradient along the filament spine outside the hub. [g] Dust temperature gradient along the entire filament:$\Delta T/\Delta l$. [h] Dust temperature gradient along the filament spine within the hub. [i] Dust temperature gradient along the filament spine outside the hub.

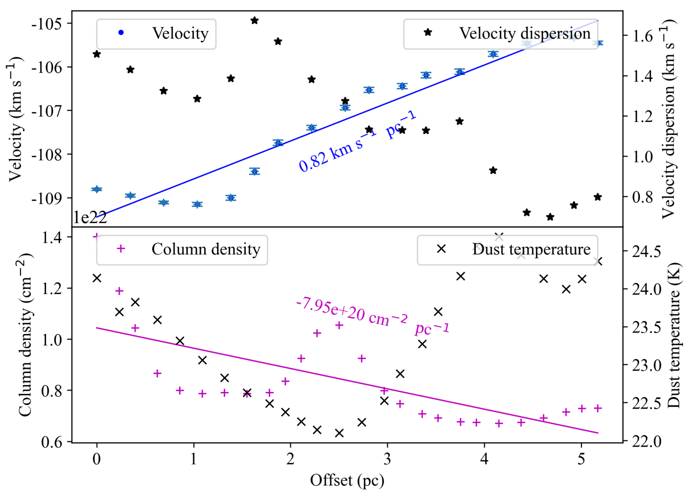

Fig. C.3. Variations in line-of-sight velocity, velocity dispersion, hydrogen molecule column density, and dust temperature along the F 4 spine.

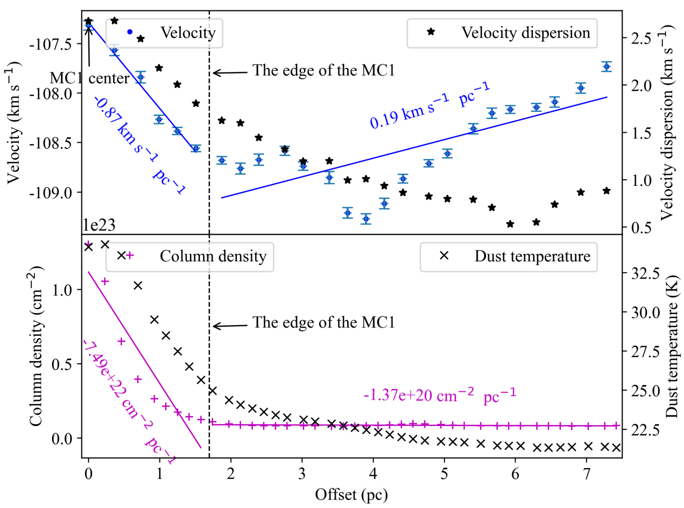

Fig. C.5. Variations in line-of-sight velocity, velocity dispersion, hydrogen molecule column density, and dust temperature along the F 6 spine, extending outward from MC 1.

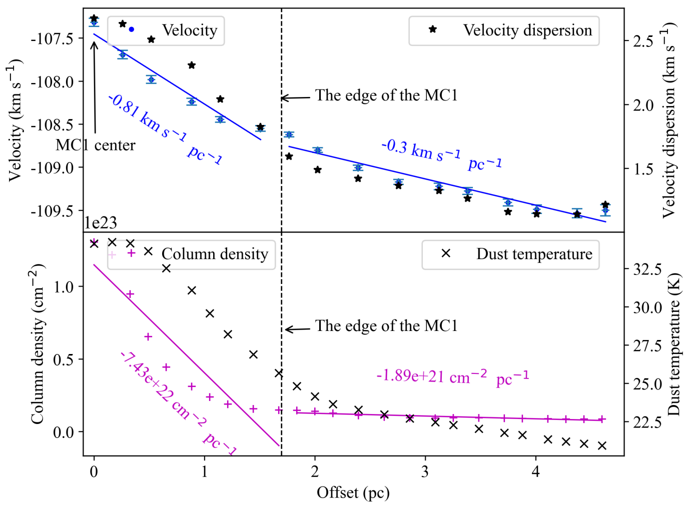

Fig. C.4. Variations in line-of-sight velocity, velocity dispersion, hydrogen molecule column density, and dust temperature along the F 5 spine, extending outward from MC 1.

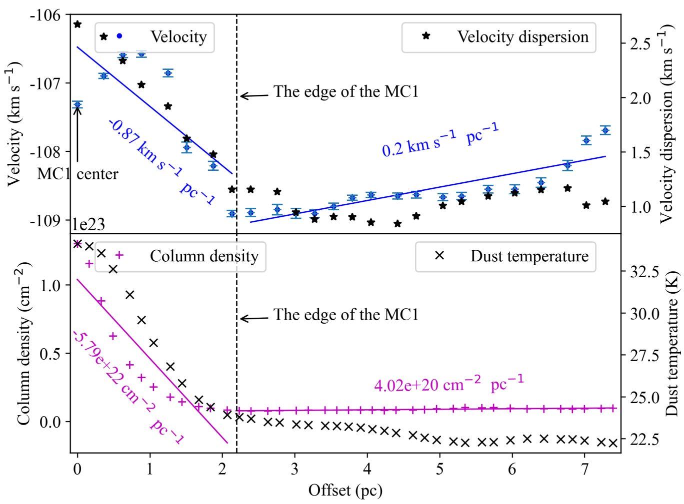

Fig. C.6. Variations in line-of-sight velocity, velocity dispersion, hydrogen molecule column density, and dust temperature along the F 7 spine, extending outward from MC 1.

Appendix D: ALMA observations of MC 1

This section presents the integrated intensity and velocity distributions of three dense molecular tracers HCN (J=1-0), $H^{13}CN$ (J=1-0), and HC_3N (J=11-10) from the ATOMS survey within MC 1.

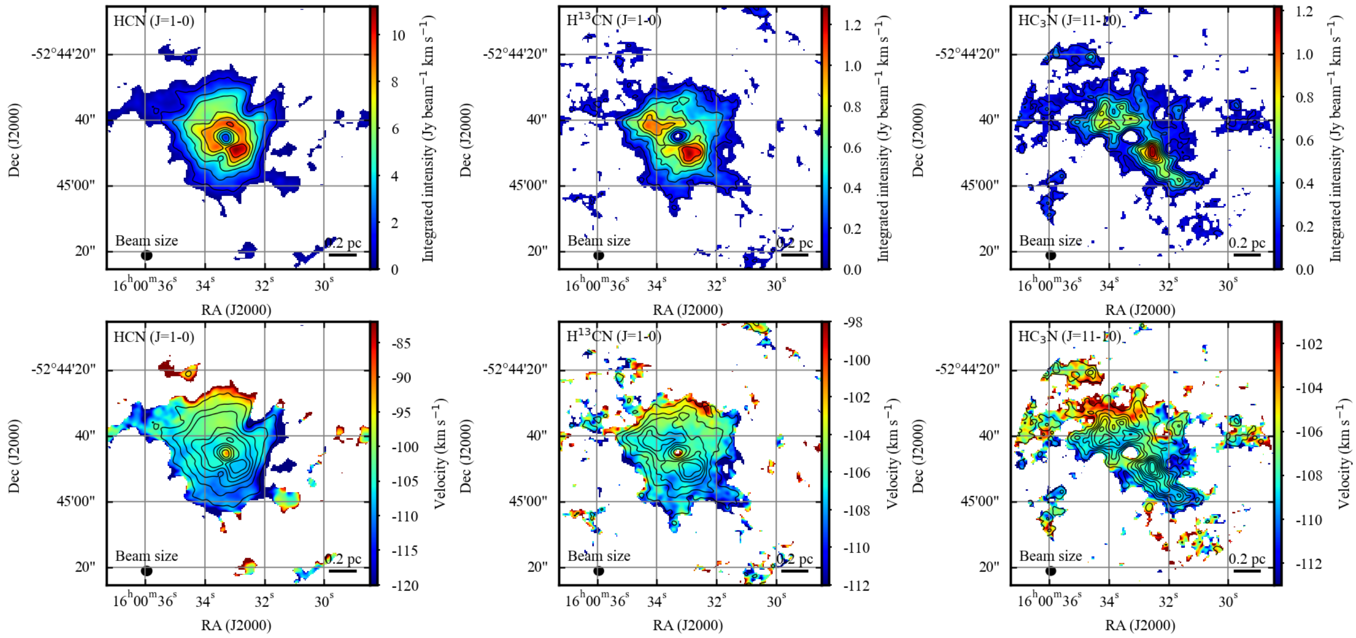

Fig. D.1. *Left panel*: Integrated intensity (top) and velocity distribution (bottom) for HCN (J=1-0). The contour lines represent the integrated intensity contours for HCN (J=1-0). *Middle panel*: Integrated intensity (top) and velocity distribution (bottom) for $H^{13}CN$ (J=1-0). The contour lines represent the integrated intensity contours for $H^{13}CN$ (J=1-0). *Right panel*: Integrated intensity (top) and velocity distribution (bottom) for HC_3N (J=11-10). The contour lines represent the integrated intensity contours for HC_3N (J=11-10).

Appendix E: The position–velocity diagram on intra-hub filaments

This section presents the P–V diagrams of the seven IHFs in MC 1. In Fig. E.1, the blue scatter points represent the velocity distribution along the spine of each filament, with the zero offset position corresponding to the convergence point of the filaments. The dashed blue lines indicate the linear fit of the velocity gradient along the filaments (see Table 3). The black scatter points represent the integrated intensity distribution of $H^{13}CO^+$ (J=1-0) along the filament spines.

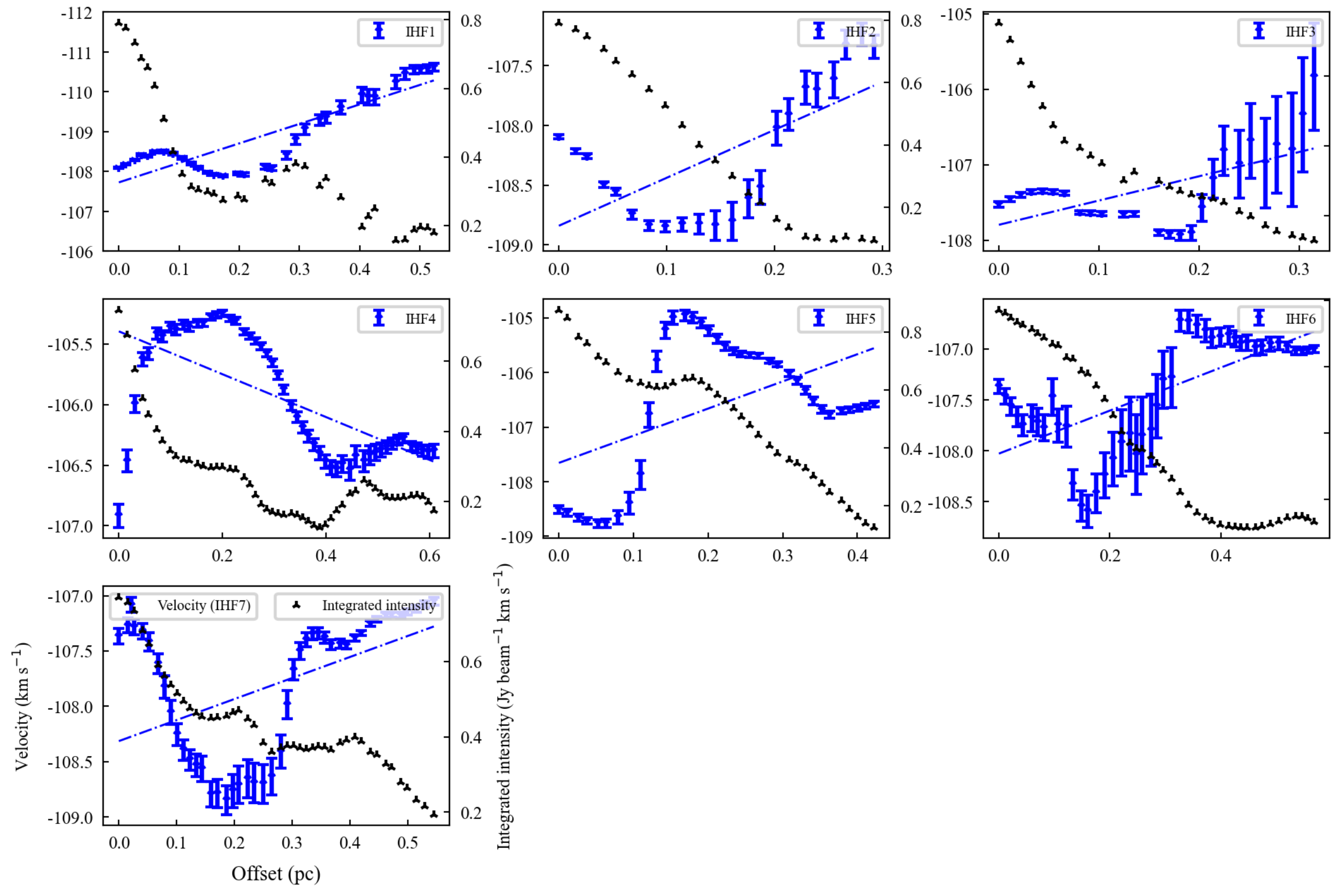

Fig. E.1. Variations in line-of-sight velocity (blue scatter points) and integrated intensity (black scatter points) along the spines of the intra-hub filaments, plotted as a function of projected distance measured outward from the adopted convergence point. The dashed blue line shows the linear fit used to estimate the projected velocity gradient.

Appendix F: Outflow structures on the SiO shell

This section presents the outflows observed using SiO (J=5-4) and ^{12}CO (J=2-1) from the ALMA-QUARKS survey. As shown in the figure below, the SiO (J=5-4) emission observed in Band 6 is primarily distributed in the northeastern field of view, exhibiting two collimated gas flows, with one side redshifted and the other blueshifted. The dark violet contours represent the 1.3 mm continuum emission, which traces compact dense continuum sources (Liu et al. 2024). Two compact continuum peaks are located near the junctions of the red and blue lobes and are likely driving sources of the two outflows (see the middle panel of Fig. F.1).

Based on the spectral distribution of ^{12}CO (J=2-1), we identified the high-velocity gas components in the red and blue lobes of one of the outflows. The intensity distributions shown in the bottom panel of Fig. F.1 were obtained by integrating the red and blue components separately and then overlaying them. The velocity ranges for the high-velocity gas in the red and blue lobes are -85 to -70 km s^{-1} and -184 to -162 km s^{-1}, respectively.

A detailed analysis of the Band 6 1.3 mm continuum emission and outflows will be conducted in future work.

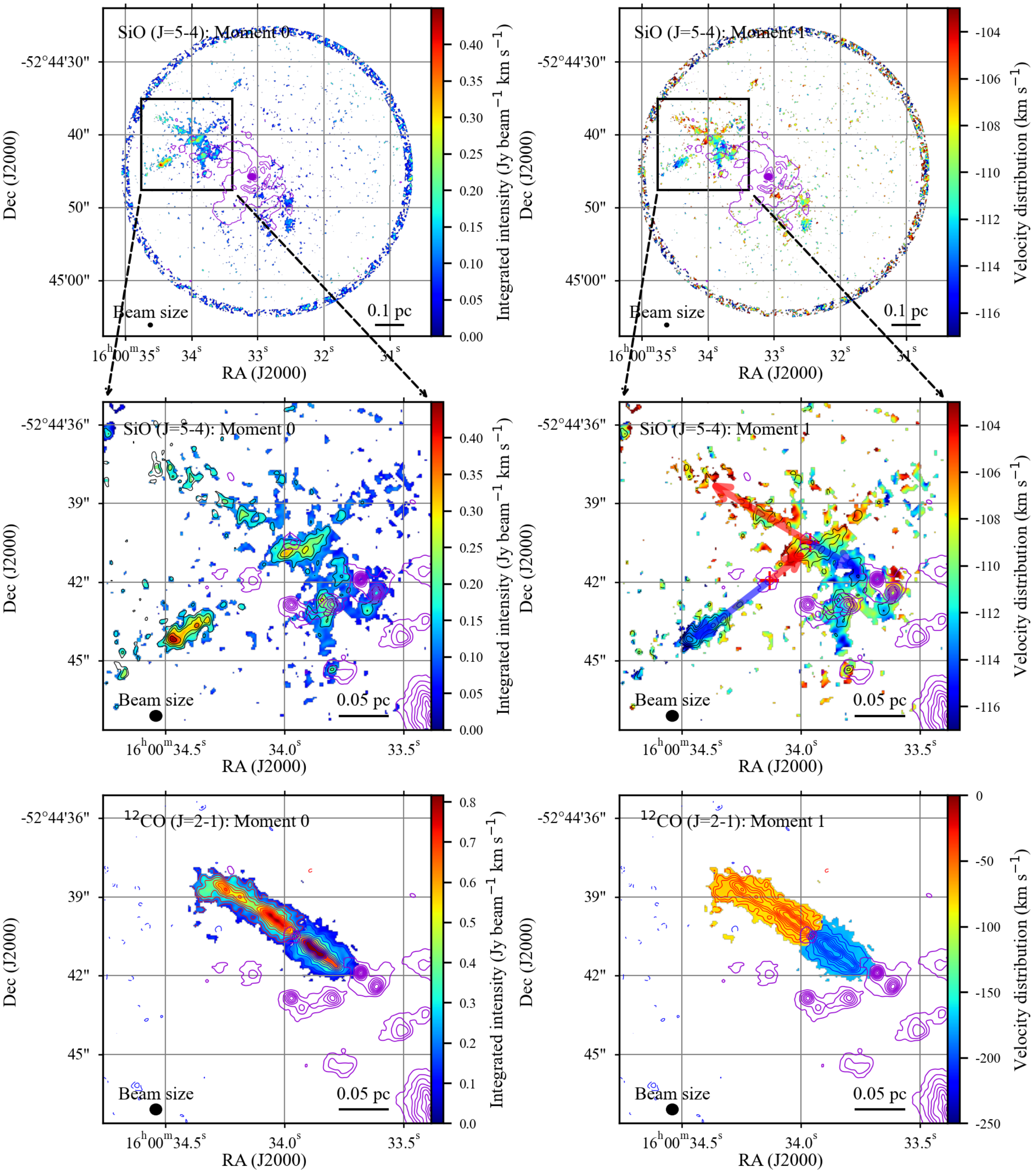

Fig. F.1. Outflows observed from SiO (J=5-4) and ^{12}CO (J=2-1). *Top panel*: Heatmaps showing the moment 0 map of SiO (J=5-4) (left) and the moment 1 map of SiO (J=5-4) (right). The dark violet contours represent the intensity distribution of 1.3 mm continuum emission. *Middle panel*: Zoomed-in view of the region highlighted by the black box in the top panel. In the right subpanel, the red and blue arrows indicate the projected directions of the redshifted and blueshifted outflow lobes, respectively, and the red plus marks the candidate outflow-driving source. *Bottom panel*: Heatmaps representing the moment 0 (left) and moment 1 (right) maps of the high-velocity gas observed in ^{12}CO (J=2-1), respectively. The red and blue contours indicate the intensity distributions of the redshifted and blueshifted outflows.